The Astrophysical Journal, 855:62 (16pp), 2018 March 1 https://doi.org/10.3847/1538-4357/aaaa72

Candidate Water Vapor Lines to Locate the H_2O Snowline through High-dispersion Spectroscopic Observations. III. Submillimeter $H_2{}^{16}O$ and $H_2{}^{18}O$ Lines

Shota Notsu[1,7], Hideko Nomura[2], Catherine Walsh[3], Mitsuhiko Honda[4], Tomoya Hirota[5], Eiji Akiyama[5], and T. J. Millar[6]

[1] Department of Astronomy, Graduate School of Science, Kyoto University, Kitashirakawa-Oiwake-cho, Sakyo-ku, Kyoto 606-8502, Japan; snotsu@kusastro.kyoto-u.ac.jp
[2] Department of Earth and Planetary Science, Tokyo Institute of Technology, 2-12-1 Ookayama, Meguro-ku, Tokyo 152-8551, Japan
[3] School of Physics and Astronomy, University of Leeds, Leeds, LS2 9JT, UK
[4] Department of Physics, School of Medicine, Kurume University, 67 Asahi-machi, Kurume, Fukuoka 830-0011, Japan
[5] National Astronomical Observatory of Japan, 2-21-1 Osawa, Mitaka, Tokyo 181-8588, Japan
[6] Astrophysics Research Centre, School of Mathematics and Physics, Queen's University Belfast, University Road, Belfast, BT7 1NN, UK
Received 2017 August 9; revised 2018 January 20; accepted 2018 January 22; published 2018 March 8

Abstract

In this paper, we extend the results presented in our former papers on using ortho-$H_2{}^{16}O$ line profiles to constrain the location of the H_2O snowline in T Tauri and Herbig Ae disks, to include submillimeter para-$H_2{}^{16}O$ and ortho- and para-$H_2{}^{18}O$ lines. Since the number densities of the ortho- and para-$H_2{}^{18}O$ molecules are about 560 times smaller than their ^{16}O analogs, they trace deeper into the disk than the ortho-$H_2{}^{16}O$ lines (down to $z = 0$, i.e., the midplane). Thus these $H_2{}^{18}O$ lines are potentially better probes of the position of the H_2O snowline at the disk midplane, depending on the dust optical depth. The values of the Einstein A coefficients of submillimeter candidate water lines tend to be lower (typically $<10^{-4}\,s^{-1}$) than infrared candidate water lines. Thus in the submillimeter candidate water line cases, the local intensity from the outer optically thin region in the disk is around 10^4 times smaller than that in the infrared candidate water line cases. Therefore, in the submillimeter lines, especially $H_2{}^{18}O$ and para-$H_2{}^{16}O$ lines with relatively lower upper state energies (∼a few 100 K) can also locate the position of the H_2O snowline. We also investigate the possibility of future observations with ALMA to identify the position of the water snowline. There are several candidate water lines that trace the hot water gas inside the H_2O snowline in ALMA Bands 5–10.

Key words: astrochemistry – ISM: molecules – protoplanetary disks – stars: formation – submillimeter: planetary systems

1. Introduction

Measuring the position of the water snowline (which corresponds to the sublimation front of water molecules, e.g., Hayashi 1981; Hayashi et al. 1985) by observations in protoplanetary disks is crucial because it will constrain the chemical and physical structures of disks (e.g., Oka et al. 2011; Banzatti et al. 2015; Piso et al. 2015, 2016; Cieza et al. 2016; Krijt et al. 2016; Pinilla et al. 2017; Schoonenberg et al. 2017), the current planetesimal and planet formation theories (e.g., Öberg et al. 2011; Okuzumi et al. 2012; Ros & Johansen 2013), and the origin of water on terrestrial planets (e.g., Morbidelli et al. 2000, 2012, 2016; Walsh et al. 2011; Ida & Guillot 2016; Sato et al. 2016; Raymond & Izidoro 2017).

It has been difficult to locate the H_2O snowline directly in protoplanetary disks through imaging observations of H_2O ice (e.g., Inoue et al. 2008; Honda et al. 2009, 2016). This is because the spatial resolution of these observations is insufficient. Water lines from disks have been detected through recent space infrared spectroscopic observations, such as *Spitzer*/IRS and *Herschel*/PACS, HIFI (for more details, see, e.g., Carr & Najita 2008, 2011; Pontoppidan et al. 2010a; Hogerheijde et al. 2011; Salyk et al. 2011; Fedele et al. 2012, 2013; Riviere-Marichalar et al. 2012; Kamp et al. 2013; Najita et al. 2013; Podio et al. 2013; Zhang et al. 2013; van Dishoeck et al. 2014; Antonellini et al. 2015, 2016, 2017; Blevins et al. 2016; Notsu et al. 2016, 2017; Banzatti et al. 2017; Du et al. 2017). However, these lines mainly trace the disk surface and the cold water gas outside the H_2O snowline.

Water line profiles were detected by ground-based near- and mid-infrared spectroscopic observations using the Keck and VLT for some bright T Tauri disks[8] (e.g., Salyk et al. 2008; Pontoppidan et al. 2010b; Mandell et al. 2012). Those observations suggested that the hot water gas resides in the inner part of the disks; however, the spatial and spectral resolution was not sufficient to investigate detailed structures, such as the position of the H_2O snowline. In addition, the observed lines, with large Einstein A coefficients, are sensitive to the water gas in the disk surface and are potentially polluted by slow disk winds.

In our former papers (Notsu et al. 2016, 2017), we proposed a means to identify the location of the H_2O snowline more directly by analyzing the Keplerian profiles of H_2O lines, which can be obtained by high-dispersion spectroscopic observations and selected based on specific criteria. We concluded that lines that have small Einstein A coefficients ($A_{ul} = 10^{-6} \sim 10^{-3}\,s^{-1}$) and relatively high upper state energies ($E_{up} \sim 1000$ K) trace the hot water reservoir inside the H_2O snowline, and can locate the position of the H_2O snowline. In these candidate lines, the contribution of the optically thick hot midplane inside the H_2O snowline is large compared with that of the outer optically thin surface layer. This is because the intensities of lines from the optically thin

[7] Research Fellow of Japan Society for the Promotion of Science (DC1).

[8] In the remainder of this paper, we define the protoplanetary disks around T Tauri/Herbig Ae stars as "T Tauri/Herbig Ae disks."

Table 1
The Central Star and Disk Parameters of Our Adopted Physical Models

Star	M_* ($M_\odot$)	R_* ($R_\odot$)	T_* (K)	$\dot{M}$ ($M_\odot$ yr^{-1})	α	g/d	$M_{\rm disk}$ ($M_\odot$)	UV Excess?
T Tauri	0.5	2.0	4000	10^{-8}	10^{-2}	100	2.4×10^{-2}	Yes
Herbig Ae	2.5	2.0	10,000	10^{-8}	10^{-2}	100	2.5×10^{-2}	No

Note: M_*: central star mass, R_*: star radius, T_*: star effective temperature, $\dot{M}$: mass accretion rate, α: viscous parameter, g/d: gas to dust mass ratio, $M_{\rm disk}$: total disk mass. UV Excess?: whether stellar UV radiation field has excess emission components, such as Lyα line emission and optically thin hydrogenic bremsstrahlung radiation.

region are proportional to the Einstein A coefficient. Moreover, the contribution of the cold water reservoir outside the H_2O snowline is also small, because lines with high excitation energies are not emitted from the regions at low temperatures. The position of the H_2O snowline of a Herbig Ae disk exists to a larger radius from the star compared with that around less massive and cooler T Tauri stars. Therefore, it is expected to be easier to observe the candidate H_2O lines, and thus identify the location of the H_2O snowline, in Herbig Ae disks than in T Tauri disks.

In this paper, we extend our water line calculations beyond ortho-$H_2{}^{16}O$ lines only to submillimeter para-$H_2{}^{16}O$ and ortho- and para-$H_2{}^{18}O$ lines. We discuss the possibility of detecting such candidate water lines to locate the position of the H_2O snowline with future observations with the Atacama Large Millimeter/Submillimeter Array (ALMA). Note that we discuss for the first time the properties of protoplanetary disk water line profiles in ALMA Band 5 (Immer et al. 2016; Humphreys et al. 2017), which is available from the second half of the observing Cycle 5 (which commenced in 2018 March). We also investigate the effects of dust emission on water line profiles. Section 2 outlines the methods. The results and discussion are described in Sections 3 and 4, respectively. In Section 5, the conclusions are listed.

2. Methods

2.1. The Disk Physical Structures and Molecular Abundances

In this paper, we adopt the molecular abundance distribution of a T Tauri disk and a Herbig Ae disk, which were calculated in Paper I (Notsu et al. 2016)[9] and Paper II (Notsu et al. 2017), using self-consistent disk physical models. Here we briefly explain our disk model.

In our works (see also Papers I and II), we used self-consistent physical models of steady, axisymmetric Keplerian disks surrounding a T Tauri star and a Herbig Ae star. They were calculated on the basis of the methods in Nomura & Millar (2005) with X-ray heating (Nomura et al. 2007). Walsh et al. (2010, 2012, 2014, 2015), Heinzeller et al. (2011), Furuya et al. (2013), and Notsu et al. (2015) adopted the same physical models to study various physical and chemical effects. Table 1 shows the central star and disk parameters of our adopted models in detail.

The gas and dust are assumed to be mixed well. In this model, we adopt a size distribution of spherical, compact dust grains that replicates the extinction curve observed in dense clouds (Mathis et al. 1977; Weingartner & Draine 2001).

In Figure 1 of Papers I and II, we displayed the gas number densities, the gas temperatures $T_{\rm g}$, the dust-grain temperatures $T_{\rm d}$, and the wavelength-integrated UV fluxes in a T Tauri disk and a Herbig Ae disk, respectively. In Section 2 of Paper II, we discussed the differences between the physical structures of the T Tauri disk and the Herbig Ae disk in detail.

The large chemical network we use to calculate the disk molecular abundances includes gas-phase reactions and gas-grain interactions (freeze-out, and thermal and nonthermal desorption). We adopt the set of atomic oxygen-rich abundances (Graedel et al. 1982; Woodall et al. 2007) as the initial elemental fractional abundances. Figure 2 of Papers I and II showed the fractional abundances (relative to total gaseous hydrogen nuclei density) of H_2O gas ($n_{\rm H_2O,gas}/n_{\rm H}$) and ice ($n_{\rm H_2O,ice}/n_{\rm H}$) in a T Tauri disk and a Herbig Ae disk.

2.2. Water Emission Line Profiles from Protoplanetary Disks

We calculate the Keplerian profiles of water emission lines from the T Tauri disk and the Herbig Ae disk, and identify those emission lines that are the best candidates for tracing emission from the inner gaseous water within the H_2O snowline. In Papers I and II, we used the same method to calculate the profiles of water emission lines from a Herbig Ae disk and a T Tauri disk (based on Rybicki & Lightman 1986; Hogerheijde & van der Tak 2000; Nomura & Millar 2005, and Schöier et al. 2005, see also Section 2.3 of Paper I). In this paper, we extend our water line calculations beyond ortho-$H_2{}^{16}O$ lines only (Papers I and II), to submillimeter para-$H_2{}^{16}O$ and ortho- and para-$H_2{}^{18}O$ lines. In addition, we focus on the submillimeter lines, in order to investigate more thoroughly the possibility of observing the H_2O snowline with ALMA.

For the calculation of line profiles, we modified the 1D code RATRAN[10] (Hogerheijde & van der Tak 2000). The data for the line parameters are adopted from the Leiden Atomic and Molecular Database LAMDA[11] (Schöier et al. 2005) for the $H_2{}^{16}O$ lines and from the HITRAN Database[12] (e.g., Rothman et al. 2013) for the $H_2{}^{18}O$ lines. We also cross-referenced the values of line parameters with the Splatalogue database.[13] The value of the ortho-to-para ratio (OPR) of water is set to 3, which is the high-temperature value (Mumma et al. 1987; Hama & Watanabe 2013; Hama et al. 2016). Here we mention that Hama et al. (2016) reported from their experiments that water desorbed from the icy dust-grain surface at 10 K shows the OPR = 3, which invalidates the assumed relation between OPR and the formation temperature of water (Mumma et al. 1987). They argue that the role of gas-phase processes

[9] In the remainder of this paper, we define Notsu et al. (2016) and Notsu et al. (2017) as Papers I and II, respectively.

[10] http://home.strw.leidenuniv.nl/~michiel/ratran/
[11] http://home.strw.leidenuniv.nl/~moldata/
[12] http://www.hitran.org
[13] http://www.cv.nrao.edu/php/splat/

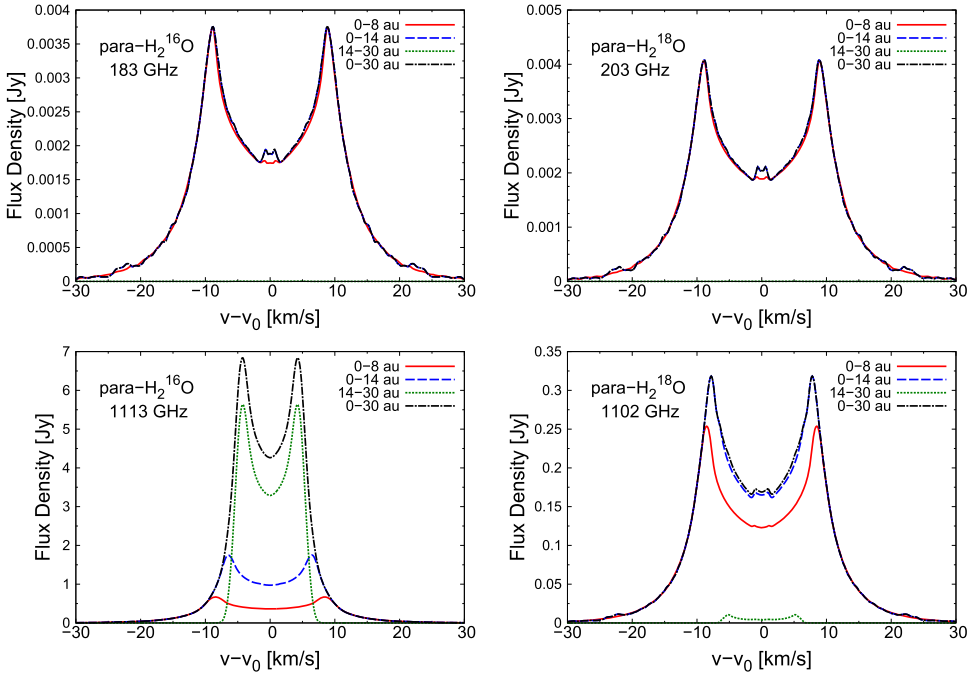

Figure 1. Profiles of para-$H_2{}^{16}O$ lines at 183 GHz (top left) and 1113 GHz (bottom left), and para-$H_2{}^{18}O$ lines at 203 GHz (top right), and 1102 GHz (bottom right) for the Herbig Ae disk. In these line profiles, we ignore dust emission and adopt a disk inclination, $i = 30°$ and the distance to the object, $d = 140$ pc. The line profiles from inside 8 au (the inner high-temperature region) are displayed with red solid lines, those from within 14 au (∼within the H_2O snowline) are blue dashed lines, those from 14–30 au (∼outside the H_2O snowline) are green dotted lines, and those from the total area inside 30 au are black dashed dotted lines. In the top two panels, the flux densities outside the H_2O snowline (green dotted lines, $<10^{-4}$ Jy) are much smaller than those inside 8 au (red solid lines). Therefore, the red solid lines, blue dashed lines, and black dashed dotted lines are almost completely overlapped (see also Figure 8).

that convert the OPR to a lower value in low temperature regions is important, though the detailed mechanism is not yet understood. We set the isotope ratio of oxygen $^{16}O/^{18}O$ to 560 throughout the disk, as Jørgensen & van Dishoeck (2010) and Persson et al. (2012) adopted. This $^{16}O/^{18}O$ value is determined by the observation of local interstellar medium (Wilson & Rood 1994). We do not include emission from jet components and disk winds in calculating the line profiles.

The assumption of local thermal equilibrium (LTE) is adopted in our calculations to obtain the level populations of the water molecule. In Section 3.2.5 of Paper I and Section 4.2 of Paper II, we discussed the validity of this assumption, and we concluded that the LTE assumption is valid when we calculate the candidate water lines that probe emission from hot gaseous water inside the H_2O snowline. This is because these lines mainly come from the dense region ($\sim 10^{11}$–10^{14} cm^{-3}) at $z/r < 0.1$ inside the H_2O snowline, while they have low values of Einstein A coefficients, such that their critical densities $n_{cr} = A_{ul}/\langle\sigma v\rangle$[14] are relatively small ($n_{cr} \sim 10^5$–10^7 cm^{-3}, see also Table 1 of Paper II). Here we note that n_{cr} of the para-$H_2{}^{16}O$ 183 GHz and 325 GHz lines are 1.4×10^5 and 1.2×10^6 cm^{-3}, respectively. These values are lower than the values of the total gas density not only in the inner disk midplane, but also in the hot surface water layer of the outer disk ($\sim 10^7$–10^8 cm^{-3}) and in the photodesorbed water layer ($\sim 10^8$–10^{10} cm^{-3}). In contrast, non-LTE effects are important for strong water lines, which have large A_{ul} ($\sim 10^{-1}$–10^0 s^{-1}), and trace the inner/outer hot surface layers (e.g., the ortho-$H_2{}^{16}O$ 63.32 μm line) or the cold photodesorbed layer (e.g., the ortho-$H_2{}^{16}O$ 557 GHz and the para-$H_2{}^{16}O$ 1113 GHz lines, see, e.g., Meijerink et al. 2009; Woitke et al. 2009; Banzatti et al. 2012; Antonellini et al. 2015, 2016).

[14] $\langle\sigma v\rangle$ is the collisional rates for the excitation of H_2O molecules by electrons and H_2 molecules for an adopted value of the collisional temperature of 200 K (Faure & Josselin 2008).

3. Results

3.1. The Velocity Profiles of Submillimeter Water Emission Lines

Figures 1 and 2 show the velocity profiles for representative characteristic para-$H_2{}^{16}O$ lines at 183 GHz (top left) and 1113 GHz (bottom left), and para-$H_2{}^{18}O$ lines at 203 GHz (top right) and 1102 GHz (bottom right) from the Herbig Ae disk and the T Tauri disk, respectively. The para-$H_2{}^{16}O$ 183 GHz line and the para-$H_2{}^{18}O$ 203 GHz line have the same transition levels and fall in ALMA Band 5 (Immer et al. 2016; Humphreys et al. 2017). The detailed parameters, such as transition quantum numbers ($J_{K_aK_c}$), wavelength λ, frequency, A_{ul}, E_{up}, and total fluxes of lines are listed in Tables 3 and 4 in the Appendix. In calculating the line profiles in Figures 1 and 2 (also Figures 7 and 8, see Section 3.4), and total fluxes in Tables 3 and 4, we do not include dust emission, although we do include both gas and dust absorption. We discuss the effects of dust emission in Section 4.1. In calculating line profiles and total fluxes in this paper (see Figures 1, 2, 7, 8, 9, and 10, and Tables 3 and 4), we adopted the inclination angle of the disk, $i = 30°$ and the distance to the object $d = 140$ pc (∼the distance of Taurus molecular cloud).

The position of the H_2O snowline in the T Tauri disk ($r \sim 1.6$ au, $T_g \sim 150$ K, see Paper I) is closer to the central star than that in the Herbig Ae disk ($r \sim 14$ au, $T_g \sim 120$ K, see Paper II), in agreement with previous studies (e.g., Woitke et al. 2009; Walsh et al. 2015). Table 2 shows the regional classifications in the disk midplane with different water

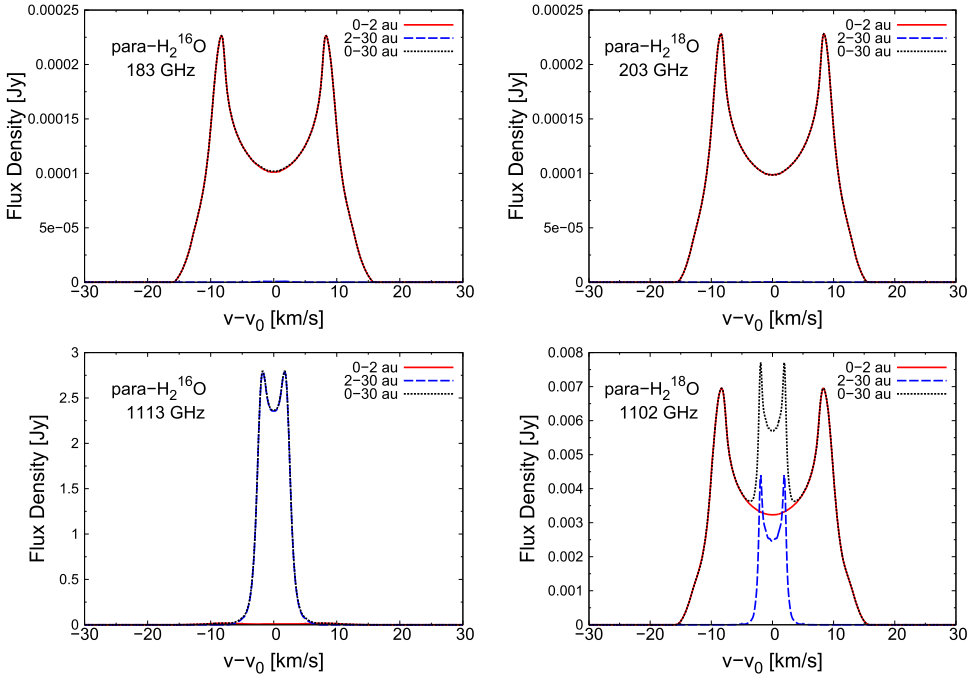

Figure 2. Same as Figure 1 but for the T Tauri disk. The line profiles from inside 2 au (∼within the H_2O snowline) are displayed with red solid lines, those from 2–30 au (∼outside the H_2O snowline) are blue dashed lines, and those from the total area inside 30 au are black dotted lines. In the top two panels, the flux densities outside the H_2O snowline (blue dashed lines, $<10^{-5}$ Jy) are much smaller than those inside the H_2O snowline (red solid lines). Therefore, the red solid lines and black dotted lines are almost completely overlapped. Moreover, in the bottom left panels, the flux densities outside the H_2O snowline (blue dashed lines) are much larger than those inside the H_2O snowline (red solid lines). Therefore, the blue dashed lines and black dotted lines are almost completely overlapped.

fractional abundances (for more details, see also Papers I and II). Inside the H_2O snowline (regions A_{TT}, A_{HA}, and B_{HA}, see also Table 2), the temperature exceeds the sublimation temperature under the pressure conditions of the midplane and most of the H_2O molecules are released into the gas-phase through thermal desorption. Thus the column densities of water gas become larger ($>10^{16}$ cm^{-2}, see Figure 3 of Paper II) than those of the outer disk ($\sim10^{14}$ cm^{-2}). In the case of Herbig Ae disks, the gas-phase chemistry to form H_2O molecules is efficient in the inner region at a higher temperature (region A_{HA}, see Table 2), and the column densities of gaseous water molecules become much larger ($\sim10^{20}$–10^{22} cm^{-2}, see Figure 3 of Paper II and Section 3.2 of this paper). Since the radial temperature profile in the midplane of the T Tauri disk is steeper than that of the Herbig Ae disk, the T Tauri disk does not have a B_{HA}-like transition region with a relaively large fractional abundance of water gas ($\sim10^{-8}$). Thus in the cases of candidate water lines with smaller Einstein A coefficients ($A_{ul} = 10^{-6} \sim 10^{-3}$ s^{-1}) and relatively high upper state energies ($E_{up} \sim 1000$ K), the contribution to the line emission of the optically thick hot midplane inside the H_2O snowline is much higher than that of the outer optically thin surface layer.

In the top panels of Figures 1 and 2, the contributions from the inner disk within the H_2O snowline (regions A_{TT}, A_{HA}, and B_{HA}, see also Table 2) are very large compared with the contributions from the outer disk (regions B_{TT}, C_{HA}, see also Table 2), and they have the characteristic Keplerian rotationally broadened double-peaked profiles. Moreover, in the line profiles from the Herbig Ae disk, most of the emission fluxes come from the high H_2O gas abundance region (region A_{HA}). The two peak positions and the rapid flux density drop between the peaks contains information on the hot H_2O gas distribution inside the H_2O snowline. The spread in the wings of the emission profile (high velocity regions) represents the inner edge of the H_2O gas distribution in the disk. This is because emission from each radial region in the disk is Doppler shifted due to the Keplerian rotation (see also Equations (11) and (12) of Paper I). Comparing submillimeter water lines having the same transition quantum numbers ($J_{K_aK_c}$), the total flux of the para-$H_2{}^{16}O$ 183 GHz line tends to be 0.8 times larger than that of the para-$H_2{}^{18}O$ 203 GHz line (see Tables 3 and 4).

Figure 3 shows the velocity profiles for the para-$H_2{}^{18}O$ lines at 203 GHz (top) and 1102 GHz (bottom) from the Herbig Ae disk inside 30 au with different inclination angles ($i = 5°$, 15°, 30°, 45°, 60°). If we observe objects with smaller/larger disk inclination angles than those of our original model value ($i = 30°$), the widths of the line peaks become smaller/larger. This is because the projected Keplerian velocity is proportional to sin i. If the object is nearly face on ($i \sim 0°$), the shape of the line profile is close to that expected from thermal broadening only, and the flux densities at the line peaks become larger. In contrast, in objects with larger disk inclination angles, the line emission components from various places in the disks are dispersed at various velocities due to the effect of Doppler shift. Thus the flux densities at the line peaks tend to be smaller as the disk inclination angles become larger. Here we note that the flux densities at the line peaks are similar in the cases of much larger inclination angles ($i > 45°$). Since the line width depends on central star mass and inclination angle of the disk, we have to know these values in advance through other observations (e.g., resolved imaging of strong molecular lines like CO lines) in order to locate the H_2O snowline from the profiles of water line emission.

In the bottom panels of Figures 1 and 2, except for the para-$H_2{}^{18}O$ 1102 GHz line for the Herbig Ae disk, the outer disk contributions (regions B_{TT}, C_{HA}, see Table 2) are large compared with that from the inner disk within the H_2O snowline (regions A_{TT}, A_{HA}, and B_{HA}, see Table 2). In addition,

Table 2
The Regional Classifications in the Disk Midplane with Different Water Abundances

Region Name	Star	r (au)	T_g (K)	$n_{H_2O,gas}/n_H$	Comments
A_{TT}	T Tauri	0–2	>150	$\sim 10^{-5}$–10^{-4}	inside the H_2O snowline
B_{TT}		2–30	<150	$\sim 10^{-12}$	outside the H_2O snowline
A_{HA}	Herbig Ae	0–8	>170	$\sim 10^{-5}$–10^{-4}	high H_2O abundance region
B_{HA}		8–14	120–170	$\sim 10^{-8}$	inside the H_2O snowline
C_{HA}		14–30	<120	$\sim 10^{-12}$	outside the H_2O snowline

Note: r: the disk radius from the central star, T_g: disk gas temperature, $n_{H_2O,gas}/n_H$: the fractional abundances (relative to total gaseous hydrogen nuclei density) of water gas.

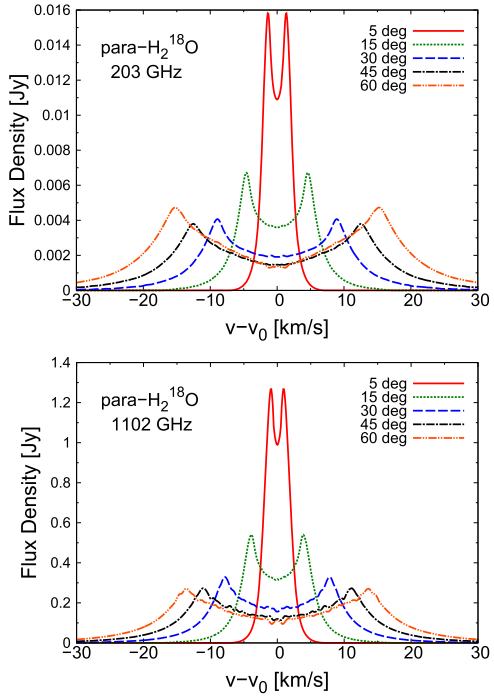

Figure 3. Velocity profiles for the para-$H_2{}^{18}O$ lines at 203 GHz (top panel) and 1102 GHz (bottom panel) from the Herbig Ae disk inside 30 au with different inclination angles, $i = 5°$ (red solid lines), 15° (green dotted lines), 30° (blue dashed lines), 45° (black dashed dotted lines), and 60° (orange dashed double dotted lines).

the widths between the line double peaks are about 2–3 times narrower than those of candidate water lines (see top panels of Figures 1 and 2), although the values of A_{ul} are not so high. This is because these water lines are the ground-state rotational transitions and have much smaller values of E_{up} (~50 K) compared to those of other lines. The fluxes of these lines mainly come from the water reservoir in the outer cold photodesorption region.

3.2. The Local Intensity and Optical Depth Distributions of Submillimeter Water Emission Lines

Figure 4 shows the water line local intensity (emissivity times line-of-sight extinction and local length, $\eta_{ul} e^{-\tau_{ul}}$ ds; see also Equation (14) of Paper I) for the Herbig Ae disk. In the left panels of Figure 4, the total (gas and dust) optical depth contours ($\tau_{ul} = 0.1$, 1, and 10) are plotted on top of the line local intensities. The gas temperature contours ($T_g = 120$, 170, 300 K) are plotted in the right-hand panels. The line-of-sight direction corresponds to $z = +\infty$ to $-\infty$ at each disk radius, thus the inclination angle is assumed to be 0°. In calculating the values of τ_{ul}, we consider the contributions of both line absorption by the water gas and absorption by dust grains. Here we note that the units in Figures 1–3 are Jy ($=10^{26}$ W m^{-2} Hz^{-1}) and the values are those observed on Earth. In contrast, we plot the "local intensity" (not "flux density") of each grid in the disk in Figure 4, and the units in this figure are W m^{-2} Hz^{-1} sr^{-1} (see also Papers I and II). Figure 5 shows the normalized cumulative line local intensity distributions along the vertical direction at $r = 5$ au (top panels), $r = 10$ au (middle panels), and $r = 30$ au (bottom panels), along with the gas temperature T_g in K. In Figure 5, we also plot the para-$H_2{}^{16}O$ 325 GHz line and the para-$H_2{}^{18}O$ 322 GHz line, which are the same transition levels and fall in ALMA Band 7. Here we note that the detailed profiles of these two lines are shown in Figure 8. Looking at the top panels of Figures 4 and all panels of Figure 5, the value of local intensities within $r < 14$ au (the position of the H_2O snowline), $T_g > 120$ K, and $z/r \lesssim 0.1$ are larger than those from the outer optically thin hot surface layer and the photodesorption region. In particular, the local intensities from the high H_2O gas abundance region (region A_{HA}) and $z/r \lesssim 0.1$ are much larger (see also Section 3.2.1 of Paper II). Here we note that these submillimeter lines have smaller A_{ul} values ($\sim 10^{-5}$–10^{-6} s^{-1}), and relatively smaller E_{up} values (~200–500 K) compared with candidate ortho-$H_2{}^{16}O$ lines, which were discussed in Papers I and II ($A_{ul} \sim 10^{-3}$–10^{-6} s^{-1}, $E_{up} \sim$ 700–2100 K). For the submillimeter $H_2{}^{18}O$ and para-$H_2{}^{16}O$ lines, since the values of A_{ul} tend to be smaller (typically $<10^{-4}$ s^{-1}) than those of infrared candidate ortho-$H_2{}^{16}O$ lines (see Paper II), and the number densities of $H_2{}^{18}O$ and para-$H_2{}^{16}O$ molecules are smaller (OPR = 3, $^{16}O/^{18}O = 560$, see also Section 2.2) than those of ortho-$H_2{}^{16}O$ molecules, contributions from the outer optically thin surface region become much smaller. In the submillimeter candidate water line cases, the local intensity from the outer optically thin disk is around 10^4 times smaller than that for the infrared candidate water line cases (see paper II). Therefore, we recommend that submillimeter $H_2{}^{18}O$ and para-$H_2{}^{16}O$ lines with relatively small values of E_{up} (~200 K) can be used for locating the position of the H_2O snowline.

The optical depths become larger as E_{up} becomes smaller (see Figure 5), because the absorption by lines is stronger even in the colder region of the disk (see also Paper II). The dust opacity at submillimeter wavelengths is small compared with those at infrared wavelengths. Hence, for the case of candidate submillimeter lines, line absorption by excited molecules mainly determines the emitting regions of lines and total

Table 3
Calculated Parameters and Total Fluxes for all Submillimeter Ortho- and Para-$H_2{}^{16}O$ Lines

$J_{K_aK_c}$	λ[a] (μm)	Frequency (GHz)	A_{ul} (s^{-1})	E_{up} (K)	HAe Flux[b] (W m^{-2})	TT Flux[c] (W m^{-2})	Comments[d]
			ortho-$H_2{}^{16}O$ lines				
6_{16}–5_{23}	13482.8594	22.23508	1.835×10^{-9}	643.5	1.4×10^{-24}	4.5×10^{-26}	
10_{29}–9_{36}[e]	933.2767	321.22568	6.165×10^{-6}	1861.2	2.3×10^{-21}	7.8×10^{-23}	ALMA Band 7
4_{14}–3_{21}	788.5180	380.19736	3.083×10^{-5}	323.5	1.7×10^{-20}	3.3×10^{-22}	
6_{43}–5_{50}[e]	682.6641	439.15079	2.816×10^{-5}	1088.7	1.4×10^{-20}	3.1×10^{-22}	ALMA Band 8
7_{52}–6_{61}[e]	676.7044	443.01835	2.231×10^{-5}	1524.8	9.5×10^{-21}	2.5×10^{-22}	ALMA Band 8
4_{23}–3_{30}	669.1780	448.00108	5.462×10^{-5}	432.1	2.6×10^{-20}	5.0×10^{-22}	ALMA Band 8
1_{10}–1_{01}[e]	538.2889	556.93599	3.497×10^{-3}	61.0	7.2×10^{-20}	1.1×10^{-20}	*Herschel*/HIFI
5_{32}–4_{41}[e]	482.9902	620.70095	1.106×10^{-4}	732.1	5.4×10^{-20}	1.0×10^{-21}	ALMA Band 9
			para-$H_2{}^{16}O$ lines				
3_{13}–2_{20}	1635.4389	183.31009	3.653×10^{-6}	204.7	4.4×10^{-22}	1.8×10^{-23}	ALMA Band 5
5_{15}–4_{22}	922.0046	325.15290	1.168×10^{-5}	469.9	1.9×10^{-21}	7.6×10^{-23}	ALMA Band 7
7_{53}–6_{60}	685.4802	437.34666	2.146×10^{-5}	1524.6	6.3×10^{-22}	2.8×10^{-23}	ALMA Band 8
6_{42}–5_{51}	636.6522	470.88890	3.483×10^{-5}	1090.3	2.0×10^{-21}	8.8×10^{-23}	ALMA Band 8
5_{33}–4_{40}	631.5554	474.68911	4.815×10^{-5}	725.1	4.5×10^{-21}	1.8×10^{-22}	ALMA Band 8
6_{24}–7_{17}	613.7112	488.49113	1.382×10^{-5}	867.3	2.1×10^{-21}	9.5×10^{-23}	ALMA Band 8
2_{11}–2_{02}	398.6426	752.03314	7.130×10^{-3}	136.9	7.8×10^{-20}	1.5×10^{-21}	
9_{28}–8_{35}	330.8216	906.20590	2.221×10^{-4}	1554.4	6.9×10^{-21}	1.5×10^{-22}	ALMA Band 10
4_{22}–3_{31}	327.2230	916.17158	5.743×10^{-4}	454.3	5.7×10^{-20}	1.5×10^{-21}	ALMA Band 10
5_{24}–4_{31}	308.9640	970.31505	9.071×10^{-4}	598.8	6.5×10^{-20}	1.7×10^{-21}	
2_{02}–1_{11}	303.4562	987.92676	5.912×10^{-3}	100.8	1.5×10^{-19}	2.9×10^{-21}	
1_{11}–0_{00}	269.2723	1113.34301	1.863×10^{-2}	53.4	2.8×10^{-18}	2.6×10^{-19}	*Herschel*/HIFI

Notes.
[a] In calculating the line wavelength values λ from the values of line frequencies, we adopt the speed of light value $c = 2.99792458 \times 10^8$ m s^{-1}.
[b] The total line flux for a Herbig Ae disk. When we calculate these line fluxes, we do not include dust emission.
[c] The total line flux for a T Tauri disk. When we calculate these line fluxes, we do not include dust emission.
[d] "ALMA Band" means that the line is within the current ALMA Band coverage. "*Herschel*/HIFI" means that the line was detected from protoplanetary disks by previous *Herschel*/HIFI observations (e.g., Hogerheijde et al. 2011; Podio et al. 2013; van Dishoeck et al. 2014; Salinas et al. 2016; Du et al. 2017).
[e] We have already reported the values for these ortho-$H_2{}^{16}O$ lines in Paper II.

optical depth profiles in the disk midplane of the inner disk with a high H_2O gas abundance (region A_{HA}). On the other hand, dust absorption mainly controls the line opacity in the disk surface and colder midplane in the outer disk. Therefore, using candidate submillimeter lines, we can detect H_2O gas closer to the midplane ($z = 0$) inside the H_2O snowline, compared with infrared lines. In the cases of the para-$H_2{}^{16}O$ lines (see Figures 4 and 5), emission from $z < 0.03$ at $r \lesssim 3$ au is not detectable. This is because the optical depth of the innermost disk midplane is high due to absorption by excited water molecules and dust grains in the upper disk layer.

Since the number densities of the para-$H_2{}^{16}O$ molecules are one-third smaller than that of ortho-$H_2{}^{16}O$ molecules, the former can trace deeper into the disk than the latter. Furthermore, because the number densities of the $H_2{}^{18}O$ molecules are around 560 times smaller than that of $H_2{}^{16}O$ molecules, $H_2{}^{18}O$ lines can trace much deeper into the disk (down to $z = 0$) than $H_2{}^{16}O$ lines, and thus $H_2{}^{18}O$ lines are better targets to extract the position of the H_2O snowline at the disk midplane. If the dust opacity of the object is much larger than that of our disk model, however, the $H_2{}^{16}O$ lines are preferred targets. We also discuss in detail the impact of dust emission in Section 4.1.

In the Herbig Ae disk (see Paper II), there was a difference between the exact H_2O snowline location ($r \sim 14$ au) and the outer edge of the hot water gas area ($r \sim 8$ au), although there was no difference between them in a T Tauri disk with the radial steeper temperature profile in the disk midplane (see also Paper I). This is because the water formation rate by gas-phase reactions strongly depends on the gas temperature. Such a water gas distribution in the Herbig Ae disk midplane was discussed in Woitke et al. (2009). Here we point out that this distribution will depend on the adopted chemical model. Eistrup et al. (2016) calculated the chemical evolution in a disk midplane under both initial atomic and molecular abundances. They reported that for molecular initial abundances, the water gas and ice fractional abundances around the H_2O snowline ($\sim 10^{-4}$) are larger than that for atomic initial abundances ($\sim 10^{-6}$).

According to our model calculations, some submillimeter candidate ortho-$H_2{}^{16}O$ lines (e.g., see also Paper II) can trace the position of the exact H_2O snowline location. In contrast, submillimeter candidate para-$H_2{}^{16}O$ lines and para-$H_2{}^{18}O$ lines discussed in this subsection mainly trace the position of the outer edge of the hot water gas area (see Figures 1, 4 and 6). The differences in the line properties come from the differences in A_{ul} and number densities among the lines.

Here we note that van Kempen et al. (2008) conducted the calculations of far-infrared $H_2{}^{16}O$ and $H_2{}^{18}O$ lines within the *Herschel*/HIFI frequency coverage for Class 0 protostar models, and suggested that higher excitation lines ($E_{up} > 150$ K) are usually dominated by emission coming from the warm inner region.

According to Figures 4 and 5, the local intensities of the para-$H_2{}^{16}O$ 1113 GHz line are similar both outside and inside the H_2O snowline for the Herbig Ae disk. However, most disk-integrated line emission comes from the outer disk on account of the larger surface area. Moreover, the line opacity in the outer disk midplane is about 10^3–10^4 times higher than those of

Table 4
Calculated Parameters and Total Fluxes for all Submillimeter Ortho- and Para-$H_2{}^{18}O$ Lines

$J_{K_aK_c}$	λ[a] (μm)	Frequency (GHz)	A_{ul} (s^{-1})	E_{up} (K)	HAe Flux[b] (W m^{-2})	TT Flux[c] (W m^{-2})	Comments[d]
			ortho-$H_2{}^{18}O$ lines				
6_{16}–5_{23}	53295.0158	5.62515	2.988×10^{-11}	640.7	1.6×10^{-27}	1.3×10^{-28}	
10_{29}–9_{36}	1180.7587	253.89816	2.806×10^{-6}	1853.5	1.2×10^{-22}	6.3×10^{-24}	ALMA Band 6
4_{14}–3_{21}	767.5026	390.60776	3.160×10^{-5}	322.0	6.6×10^{-21}	1.9×10^{-22}	ALMA Band 8
4_{23}–3_{30}	613.0045	489.05426	6.951×10^{-5}	429.6	1.2×10^{-20}	3.4×10^{-22}	ALMA Band 8
6_{43}–5_{50}	576.3718	520.13732	4.609×10^{-5}	1080.6	5.6×10^{-21}	2.2×10^{-22}	
7_{52}–6_{61}	555.2782	539.89596	3.982×10^{-5}	1512.4	2.6×10^{-21}	1.0×10^{-22}	
1_{10}–1_{01}	547.3897	547.67644	3.257×10^{-3}	60.5	4.2×10^{-20}	1.0×10^{-21}	
5_{32}–4_{41}	433.1766	692.07914	1.511×10^{-4}	727.6	2.4×10^{-20}	7.2×10^{-22}	ALMA Band 9
			para-$H_2{}^{18}O$ lines				
3_{13}–2_{20}	1473.8514	203.40752	4.813×10^{-6}	203.7	5.2×10^{-22}	2.3×10^{-23}	ALMA Band 5
5_{15}–4_{22}	929.6894	322.46517	1.060×10^{-5}	467.9	1.4×10^{-21}	6.6×10^{-23}	ALMA Band 7
6_{24}–7_{17}	579.6653	517.18196	1.491×10^{-5}	865.0	1.5×10^{-21}	7.4×10^{-23}	
7_{53}–6_{60}	561.9372	533.49817	3.841×10^{-5}	1512.1	5.9×10^{-22}	2.5×10^{-23}	
5_{33}–4_{40}	557.9220	537.33757	6.870×10^{-5}	720.2	5.0×10^{-21}	2.1×10^{-22}	
6_{42}–5_{51}	540.3030	554.85987	5.616×10^{-5}	1082.2	2.2×10^{-21}	9.8×10^{-23}	
2_{11}–2_{02}	402.2331	745.32020	6.759×10^{-3}	136.4	6.8×10^{-20}	1.4×10^{-21}	
9_{28}–8_{35}	349.8796	856.84463	1.711×10^{-4}	1548.0	2.8×10^{-21}	7.7×10^{-23}	ALMA Band 10
4_{22}–3_{31}	308.9777	970.27204	6.759×10^{-4}	452.4	5.5×10^{-20}	1.6×10^{-21}	
2_{02}–1_{11}	301.3974	994.67513	5.970×10^{-3}	100.6	1.4×10^{-19}	2.9×10^{-21}	
5_{24}–4_{31}	298.8131	1003.27760	9.714×10^{-4}	595.9	5.7×10^{-20}	1.7×10^{-21}	
1_{11}–0_{00}	272.1185	1101.69826	1.769×10^{-2}	52.9	2.1×10^{-19}	4.4×10^{-21}	

Notes.
[a] In calculating the line wavelength values λ from the values of line frequencies, we adopt the speed of light value $c = 2.99792458 \times 10^8$ m s^{-1}.
[b] The total line flux for a Herbig Ae disk. When we calculate these line fluxes, we do not include dust emission.
[c] The total line flux for a T Tauri disk. When we calculate these line fluxes, we do not include dust emission.
[d] "ALMA Band" means that the line is within the current ALMA Band coverage. $H_2{}^{18}O$ lines have not been detected from protoplanetary disks by previous *Herschel*/HIFI observations (e.g., Hogerheijde et al. 2011; Podio et al. 2013; van Dishoeck et al. 2014; Salinas et al. 2016; Du et al. 2017).

the candidate H_2O lines with similar line wavelengths and thus similar dust opacities.

Here we note that in the case of the para-$H_2{}^{18}O$ line at 1102 GHz for the Herbig Ae disk, the contribution from the inner optically thick layer within the H_2O snowline is still dominant (see Figure 4). This is because the number densities of para-$H_2{}^{18}O$ molecules are much smaller than those of $H_2{}^{16}O$ molecules. However, the emitting region of this line extends farther into the outer disk (see also Section 3.3). Thus the contribution of the outer disk is expected to be larger if we integrate emission components within a larger disk radius (e.g., $r \lesssim$ hundreds of astronomical units). Therefore, we see that these two lines are not appropriate to detect the hot water emission inside the H_2O snowline, as concluded also for the ortho-$H_2{}^{16}O$ 557 GHz line (see Papers I and II).

3.3. The Normalized Radial Cumulative Line Fluxes

The top two panels of Figure 6 show the normalized cumulative fluxes in the radial directions of three para-$H_2{}^{16}O$ lines at 183, 325, and 1113 GHz, and the bottom two panels show those of para-$H_2{}^{18}O$ lines at 203, 322, and 1102 GHz, for the Herbig Ae disk. For the candidate $H_2{}^{16}O$ and $H_2{}^{18}O$ lines, most line flux is emitted from the region with a high water gas abundance ($\sim 10^{-5}$–10^{-4}, $r < 8$ au). For the para-$H_2{}^{16}O$ 1113 GHz line case, the line emitting region is much further out from the position of H_2O snowline ($r \sim$ 50–300 au), and it is similar to that of the ortho-$H_2{}^{16}O$ 557 GHz line (see Paper II).

Here we point out that line emission from the para-$H_2{}^{18}O$ 1102 GHz line is both from the region inside ($r < 14$ au) and much further out ($r > 100$ au) than the position of the H_2O snowline. We also discussed this line property in the last paragraph of Section 3.2.

3.4. The Properties of all Other Submillimeter Water Emission Lines

Figure 7 shows the total fluxes of all calculated submillimeter ortho- and para-$H_2{}^{16}O$ lines and ortho- and para-$H_2{}^{18}O$ lines from a Herbig Ae disk (left panels) and a T Tauri disk (right panels). The detailed line parameters and total line fluxes of $H_2{}^{16}O$ lines and $H_2{}^{18}O$ lines in Figure 7 are listed in Tables 3 and 4, respectively. In calculating the total fluxes in Figure 7 and Tables 3 and 4, we do not include dust emission, although we do include both gas and dust absorption. In Figure 7 and Tables 3 and 4, we calculated the two ground-state rotational transitions of the para-$H_2{}^{16}O$ and para-$H_2{}^{18}O$ lines (at 1113 GHz and 1102 GHz, respectively). We also include all submillimeter ortho- and para-$H_2{}^{16}O$ lines and ortho- and para-$H_2{}^{18}O$ lines with $E_{up} < 2000$ K and with a frequency of $\nu \leqslant 1003$ GHz ($\lambda \geqslant 297$ μm).

On the basis of Figure 7 and Tables 3 and 4, the values of these line fluxes from the Herbig Ae disk are about (1–5) $\times 10^2$ larger than those of the T Tauri disk. This is because the H_2O snowline position in the T Tauri disk is at a smaller radial distance than that in the Herbig Ae disk. The total line fluxes tend to be larger as the values of E_{up} are smaller and A_{ul} are larger. In addition, they tend to be smaller as the wavelengths of these water lines are longer, because mid-infrared wavelengths are the peak wavelengths of the

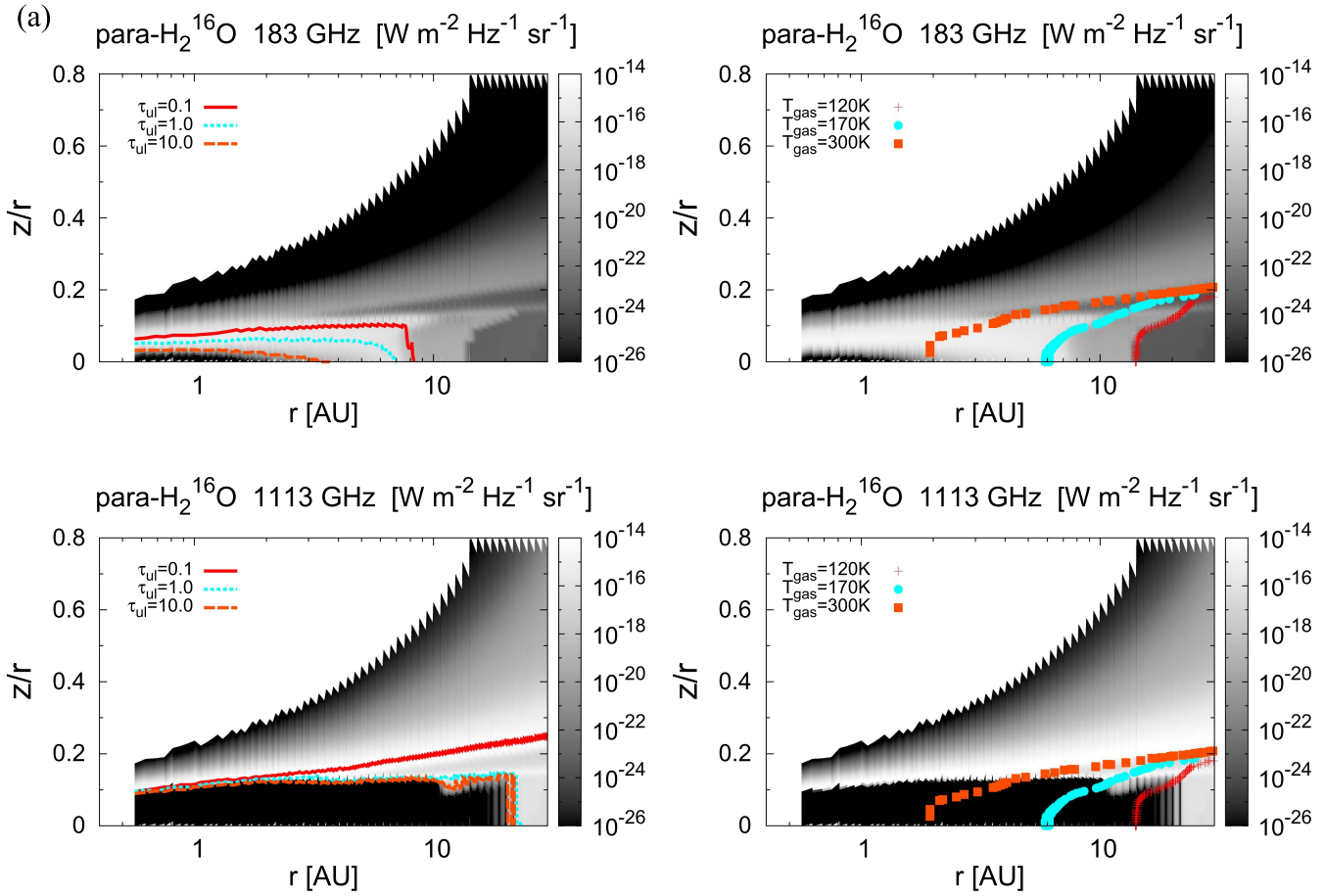

Figure 4. (a) The local intensity distributions along the line-of-sight direction of para-$H_2{}^{16}O$ lines at 183 GHz (top panels) and 1113 GHz (bottom panels) for the Herbig Ae disk. In the left panels, the total (gas and dust) optical depth contours for $\tau_{ul} = 0.1$ (red solid lines), 1 (cyan dotted lines), and 10 (orange dashed lines) are plotted on top of the line local intensities. The gas temperature contours for $T_g = 120$ K (red cross points), 170 K (cyan circle points), and 300 K (orange square points) are plotted in the right panels. The units of the local intensity are W m^{-2} Hz^{-1} sr^{-1}. (b) The local intensity distributions along the line-of-sight direction of para-$H_2{}^{18}O$ lines at 203 GHz (top panels) and 1102 GHz (bottom panels) for the Herbig Ae disk.

Planck function at the gas temperatures around the H_2O snowline ($T_g \sim 100$–200 K). Furthermore, comparing water lines with the same transition quantum numbers ($J_{K_aK_c}$), the total fluxes of $H_2{}^{16}O$ lines tend to be 0.5–10^2 times larger than those of $H_2{}^{18}O$ lines, and the flux ratios tend to be larger in the cases of ortho-H_2O lines. The differences in flux ratios are mainly due to the differences in emitting regions.

Figure 8 shows the velocity profiles of several water lines in the frequency range 300–700 GHz for the Herbig Ae disk. The values of E_{up} ($\sim$300–700 K) of lines in Figure 8 are smaller than those of candidate ortho-$H_2{}^{16}O$ lines discussed in Papers I and II ($E_{up} \sim 1000$ K). In these cases, contributions from the relatively high water gas abundance region ($\sim 10^{-8}$, $r \sim$ 8–14 au) dominate. By contrast, in the case of para-$H_2{}^{16}O$ and $H_2{}^{18}O$ lines, most of the flux comes from the high H_2O gas abundance region ($\sim 10^{-5}$–10^{-4}, $r < 8$ au), since the number densities of $H_2{}^{18}O$ and para-$H_2{}^{16}O$ molecules are smaller than those of ortho-$H_2{}^{16}O$ molecules.

4. Discussion

4.1. Influence of Dust Emission on Water Line Properties

Figure 9 shows the velocity profiles of several para-$H_2{}^{16}O$ and para-$H_2{}^{18}O$ lines for a Herbig Ae disk inside 30 au. In the line profiles with red solid lines, we do not include dust emission components (see also Figures 1 and 8). In the line profiles with blue dashed lines, we include both dust and gas emission components, and then we subtract dust emission components (the values of fluxes at $v - v_0 = \pm\infty$) after the calculation to show the line emission more clearly.

According to the red solid lines and blue dashed lines in Figure 9, if we do not include dust emission, the values of line peak flux densities become 1.1–2 times larger. This is because the column density of the inner disk is very high so that the line becomes optically thick. The position of $\tau_{ul} = 1$ at the line center in the z direction is higher than those at line-free frequencies, and the total intensity of dust emission is smaller at the line center than those at line-free frequencies. Therefore, the line flux density relative to the flux density of dust emission becomes lower, compared with the case in which both the line and dust continuum emission are optically thin, such as found for molecular clouds. Here we note that in the inner hot disk midplane at $r < 7$–8 au, the vertically integrated column densities of gaseous water molecules are $\sim 10^{20}$–10^{22} cm^{-2} (see also Figure 3 of Paper II), and the values of dust optical depth at $z \sim 0$ are around 0.05–0.4 at 183 GHz, and around 0.1–0.8 at 325 GHz. The shapes of line profiles are similar among Figures 1, 8, and 9.

In the line profiles with black dotted lines in Figure 9, we also include both dust and gas components in the same way as those with blue dashed lines, but we artificially increase the

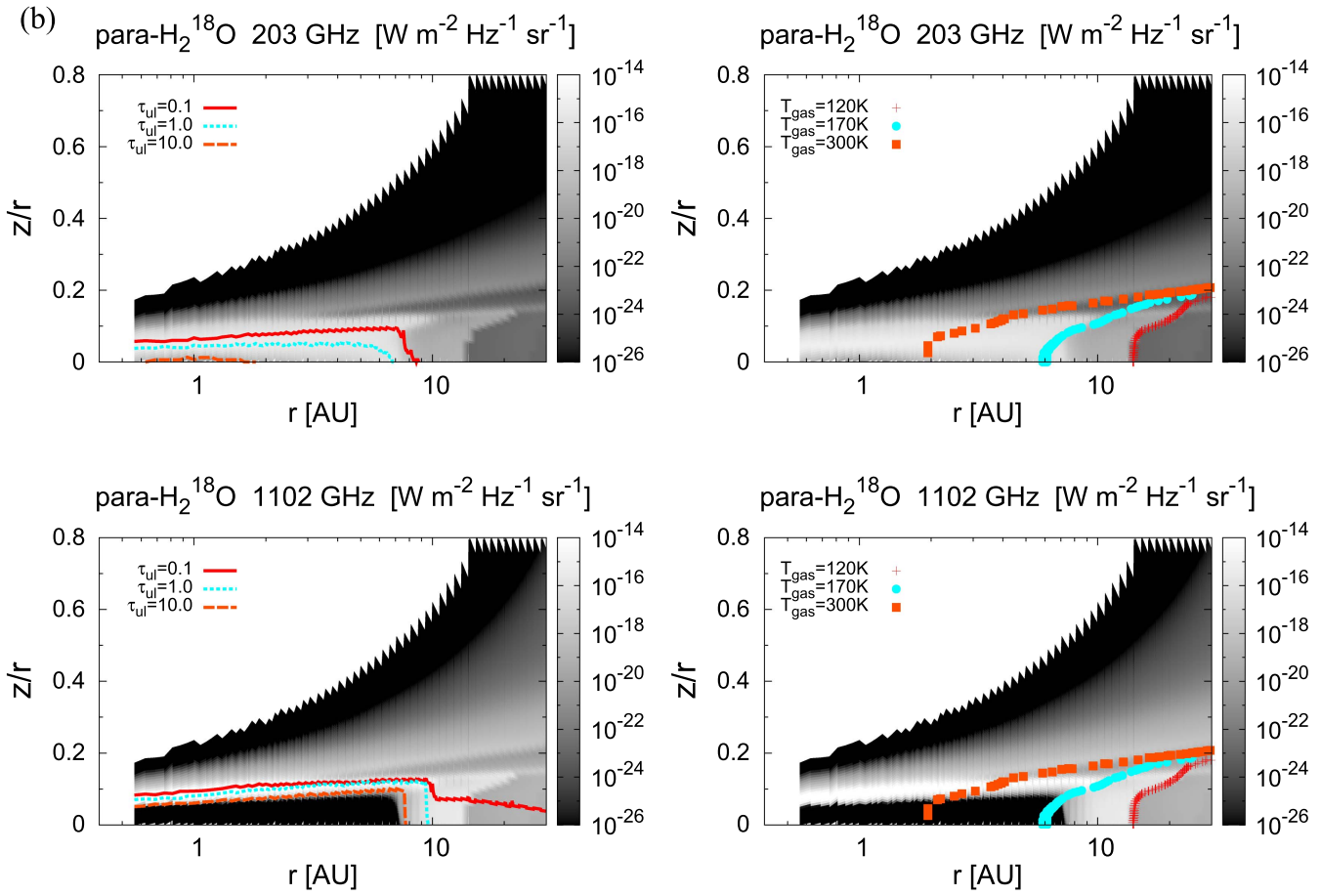

Figure 4. (Continued.)

values of dust opacity $\kappa_{\rm ul}$ by a factor of 10 in order to investigate the influence of dust opacity on line properties. We note that the dust opacity at submillimeter wavelengths changes by a factor of around 10, depending on the properties of the dust grains (e.g., Miyake & Nakagawa 1993; Draine 2006). In our fiducial disk model, dust opacities appropriate for the dark cloud model are used and they are relatively small at submillimeter wavelengths, compared with the model with grain growth (see, e.g., Nomura & Millar 2005; Aikawa & Nomura 2006, and Paper I). We again subtract dust emission components to show the line emission more clearly. The disk physical structure is the same as the original reference model. In these cases with larger values of dust opacity (see black dotted lines in Figure 9), the effect of the dust emission becomes stronger and the values of peak line flux densities become around 0.1–0.6 times smaller.

The differences in line flux densities are larger in the cases of Band 7 water lines when compared with Band 5 water lines (see Figure 9). This is because the dust opacity becomes larger as the line frequency increases (e.g., Miyake & Nakagawa 1993; Nomura & Millar 2005; Draine 2006). In addition, the differences in line flux densities are also larger in the cases of $H_2{}^{18}O$ lines, compared with $H_2{}^{16}O$ lines. The emitting regions of $H_2{}^{18}O$ lines are closer to the disk midplane (down to $z = 0$) than those of $H_2{}^{16}O$ lines. The temperature is higher, as the disk height is higher (see Figure 5) and thus the temperature around $\tau_{\rm ul} \sim 1$ of $H_2{}^{16}O$ lines is higher than those of $H_2{}^{18}O$ lines. Therefore, the line intensities are larger in the cases of $H_2{}^{16}O$ lines, compared with the cases of $H_2{}^{18}O$ lines. Thus, if the dust opacity of the disk is much larger than that of our disk model, the $H_2{}^{16}O$ lines and Band 5 lines are better candidates for submillimeter detection of the inner water reservoir. Moreover, the differences in line flux densities of para-$H_2{}^{16}O$ 1113 GHz and para-$H_2{}^{18}O$ 1102 GHz are smaller than other water lines. This is because the main line emitting region of these lines is the cold water gas of the outer photodesorption region where the dust opacity is much smaller than that in the inner disk, and where also the line intensity is greater (see also Section 3.1). Since all $H_2{}^{16}O$ and $H_2{}^{18}O$ lines treated here are optically thick (see Figure 4) and the temperature is higher as the disk height is higher (see Figure 5), line emission is stronger than dust emission, even for the case with an assumed large dust opacity.

We point out that previous mid- and near-infrared observations for Herbig Ae disks have not yet detected water line emission from the inner disk surface (Pontoppidan et al. 2010a; Fedele et al. 2011; Salyk et al. 2011), although far-infrared water lines have been detected for a few bright Herbig Ae disks (Fedele et al. 2012, 2013; Meeus et al. 2012), which are classified as group II Herbig Ae stars (e.g., Honda et al. 2015). Several explanations (e.g., inner holes/gaps, strong UV radiation fields in the disk surface, and strong infrared dust emission in the infrared wavelengths, see Section 4.3 of Paper II and Antonellini et al. 2015, 2016) have been considered responsible for this nondetection toward Herbig Ae disks. In contrast, since the dust continuum fluxes in the submillimeter wavelengths are low, the possibility of water line detections from protoplanetary disks is expected to be higher.

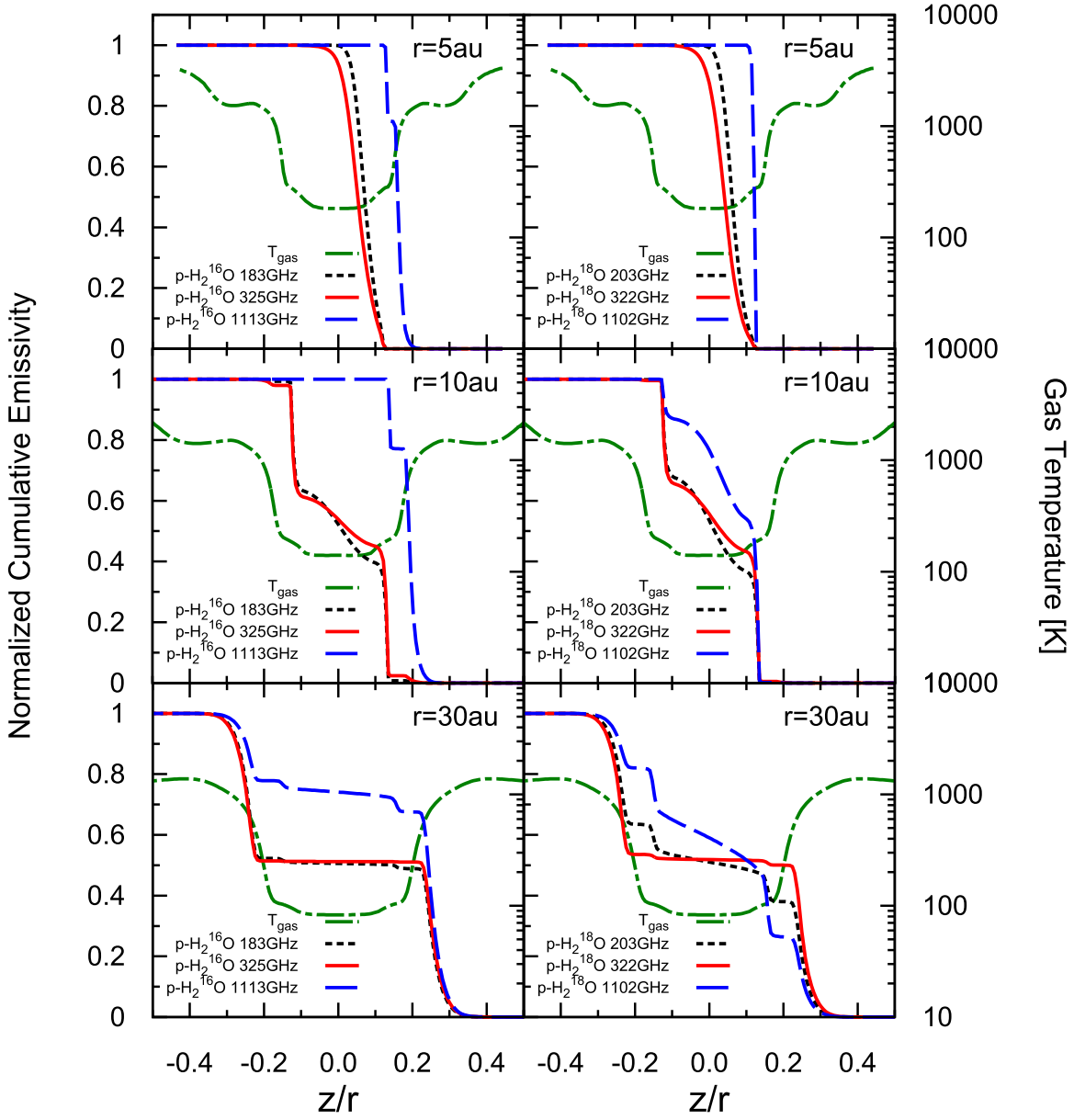

Figure 5. Normalized cumulative line local intensity distributions along the vertical direction at $r = 5$ au (top panels), $r = 10$ au (middle panels), and $r = 30$ au (bottom panels), and the vertical distribution of the gas temperature T_g [Kelvin] (green dashed dotted lines). The distributions for three para-$H_2{}^{16}O$ lines at 183 GHz (black dotted lines), 325 GHz (red solid lines), 1113 GHz (blue dashed lines) from a Herbig Ae disk are shown in the left three panels. The distributions for three para-$H_2{}^{18}O$ lines at 203 GHz (black dotted lines), 322 GHz (red solid lines), and 1102 GHz (blue dashed lines) from a Herbig Ae disk are shown in the right three panels. The cumulative local intensities are normalized using the values at $z = -\infty$.

Here we note that the para-$H_2{}^{16}O$ 1113 GHz line and ortho-$H_2{}^{16}O$ 557 GHz line were detected from disks around two T Tauri stars, TW Hya and DG Tau, and a Herbig Ae star, HD 100546 through space spectroscopic observations with *Herschel*/HIFI (e.g., Hogerheijde et al. 2011; Podio et al. 2013; Zhang et al. 2013; van Dishoeck et al. 2014; Salinas et al. 2016; Du et al. 2017). Du et al. (2017) reported the upper limit flux values of these ground level $H_2{}^{16}O$ lines for disks around two other T Tauri stars (AA Tau, DM Tau) and a Herbig Ae star (HD 163296). From the properties of lines detected by previous observations and other modeling works (e.g., Meijerink et al. 2008; Woitke et al. 2009; Antonellini et al. 2015), the main line emitting region is the cold outer disk, consistent with our results. The number of detections is smaller than those expected from previous modeling works (e.g., Antonellini et al. 2015). Du et al. (2017) discussed the reasons for the low detection rate, and proposed that gas-phase oxygen bearing molecules (such as water and CO) were removed from the line emitting layers of the outer disk by freeze-out onto dust grains followed by grain growth and settling/migration.

4.2. Influence of Different Snowline Positions and Velocity Resolution of the Line Profiles

Our model, which has a continuous disk in the radial direction and no inner gap and/or hole, is applicable to group II Herbig Ae stars (e.g., Honda et al. 2015). For a model having an inner hole (i.e., group I Herbig Ae stars), the fluxes of the H_2O lines, especially from the hot water gas within the H_2O snowline, are expected to decrease. In addition, if we adopt

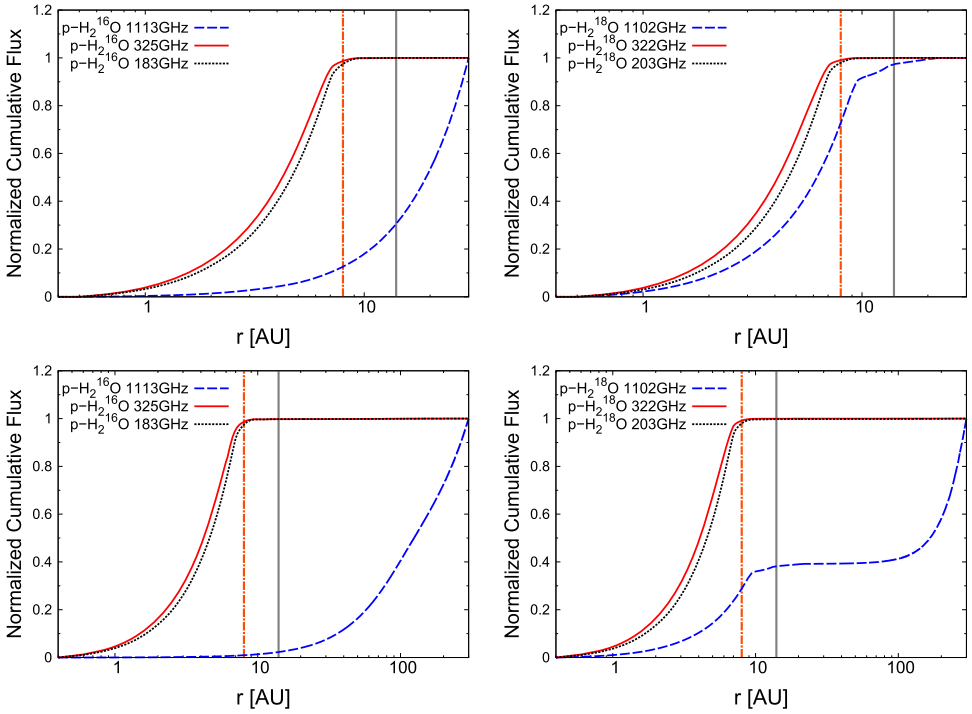

Figure 6. (Left two panels) The distributions of the normalized cumulative fluxes along the radial directions of three para-$H_2{}^{16}O$ lines at 183 GHz (black dotted lines), 325 GHz (red solid lines), and 1113 GHz (blue dashed lines) from a Herbig Ae disk. (Right two panels) The radial distributions of the normalized cumulative fluxes of three para-$H_2{}^{18}O$ lines at 203 GHz (black dotted lines), 322 GHz (red solid lines), and 1102 GHz (blue dashed lines) from the Herbig Ae disk. The vertical straight lines display the positions of r = 14 au (gray solid line) and 8 au (orange dashed dotted line), respectively. The cumulative fluxes are normalized using the values at r = 30 au (top panels) and at r = 300 au (bottom panels).

different values of dust opacities (due to dust evolution), mass accretion rates (which determine the effects of viscous heating), and central star temperatures, the position of the H_2O snowline is also changed (e.g., Oka et al. 2011; Harsono et al. 2015; Piso et al. 2015). In Section 3.2.4 of Paper I and Sections 4.1 and 4.3 of Paper II, the uncertainties in predictions of our model were presented in detail, and the water line properties for some cases in which we artificially changed of H_2O gas distribution were discussed (see Figures 8 and 9 of Paper I). If the H_2O snowline is farther from the star, and the fractional water gas abundance in the surface of the outer disk is lower than that in the original disk model, the line fluxes from the hot region within the H_2O snowline are larger than those from the cooler outer disk.

In the cases of submillimeter para-$H_2{}^{16}O$ lines and $H_2{}^{18}O$ lines, the emission fluxes from the optically thin disk surface and photodesorption region are smaller than those of ortho-$H_2{}^{16}O$ lines (see Section 3.1). Therefore, the variations in fractional water abundances in those regions will have little impact on the profiles of the para-$H_2{}^{16}O$ lines and $H_2{}^{18}O$ lines with smaller values of A_{ul} ($<10^{-4}\,s^{-1}$) and relatively higher values of E_{up} ($\gtrsim$200 K). Here we discuss the behavior of these lines in which we reduce the velocity resolution and artificially change the distribution of H_2O gas in the disk midplane, and test the validity of our model predictions.

In Figure 10, we display the profiles of the para-$H_2{}^{18}O$ line at 203 GHz from a Herbig Ae disk inside 30 au with a reduced velocity resolution ($\Delta v = 1.0\,km\,s^{-1}$). The velocity resolution we adopted in this figure is 10 times larger than those of other line profiles in this paper and our previous papers ($\Delta v = 0.1\,km\,s^{-1}$, see also Papers I and II), and a velocity resolution of 0.1–1.0 $km\,s^{-1}$ is often adopted for ALMA observations. The red solid line with cross symbols is the line profile of our original Herbig Ae disk model (see also Figure 9). In other plots, we artificially change the outer edge of the region with high H_2O water gas abundance ($=10^{-5}$) to 5 au ($T_g \sim 180$ K), 11 au ($T_g \sim 135$ K), and 14 au ($T_g \sim 120$ K). Since this line is mainly emitted from the region with a high water gas abundance ($\sim10^{-5}$–10^{-4}, see also Figures 4, 6, 8, and 9) in the Herbig Ae disk, we changed the outer edge of the region with a high H_2O water gas abundance (originally 8 au, see also Table 2).

According to Figure 10, as the region with a high water gas abundance becomes larger, the flux density of the line peaks becomes larger, and the line width, especially the width between the two peaks becomes narrower. In the outer disk, the changes in local velocity widths are smaller, since the velocity widths are inversely proportional to the square root of the radial distance of the emitting region from the central star (see also Equations (11) and (12) of Paper I). The figure shows that we will be able to distinguish the differences of the outer edge positions (or the positions of the H_2O snowline) with the resolution of a few astronomical units through observing the separation between the two peaks in the line profile with the velocity resolution of $\Delta v = 1.0\,km\,s^{-1}$ for the Herbig Ae disk with the inclination angle of 30°. Future detailed calculations, which consider the noise expected in actual observations and the errors of physical parameters such as central star masses and disk inclination angles (obtained by other previous observations), are also important to investigate the observational possibilities with ALMA.

Here we note that the disk physical structure is the same as the original reference model (see Section 2.1), because calculating several different disk physical structures and chemical structures self-consistently is computationally

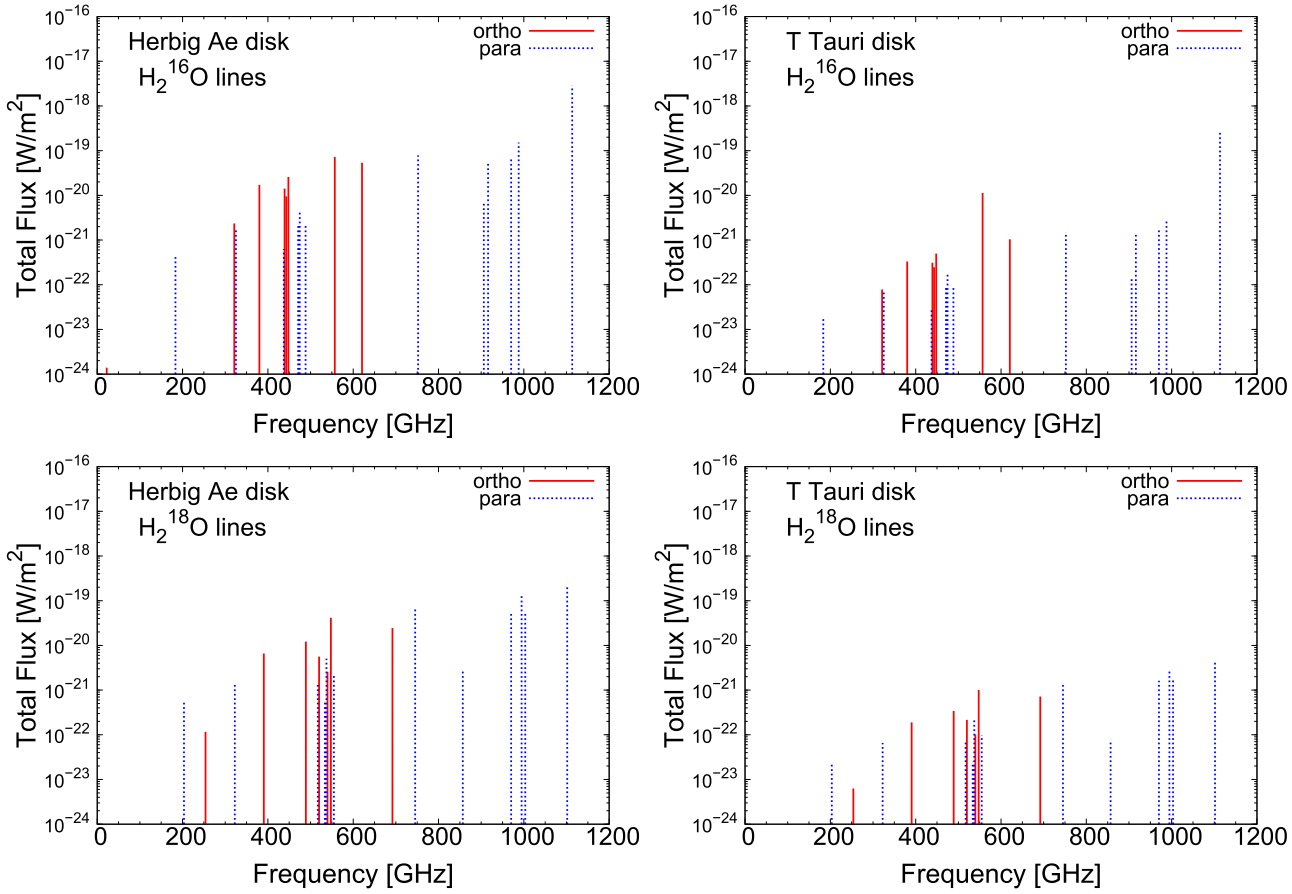

Figure 7. Disk-integrated emergent fluxes of submillimeter ortho- and para-$H_2{}^{16}O$ lines (top panels), and ortho- and para-$H_2{}^{18}O$ lines (bottom panels), from a Herbig Ae disk (left panels) and a T Tauri disk (right panels). The ortho- and para-water lines are plotted with red solid lines and blue dotted lines, respectively. These water lines are selected on the basis of their excitation energies, $0 < E_{up} < 2000$ K, and lower frequencies, $\nu = 0$–1003 GHz ($\lambda > 297$ μm). In these panels, we also plot the total fluxes of the ground-state rotational transitions of the para-$H_2{}^{16}O$ 1113 GHz line and para-$H_2{}^{18}O$ 1102 GHz line.

demanding and beyond the scope of this work. Even if we adopt self-consistent models, we expect that the line widths will not be affected; however, we do expect that line fluxes will be affected by about 0.5–4 times since the temperature of line emitting regions will be about 0.7–1.2 times different, on the basis of the differences in gas temperatures around the outer edges of high water gas abundance regions (see also Section 3.2.4 of Paper I).

4.3. Requirements for Future Observations

In order to trace the hot water gas inside the H_2O snowline, high-dispersion spectroscopic observations ($R = \lambda/\delta\lambda >$ tens of thousands) of the water candidate lines in Tables 3 and 4 are needed. This is because the velocity width between the peaks is $\sim$15–20 km s^{-1}. The para-$H_2{}^{16}O$ 183 GHz line and para-$H_2{}^{18}O$ 203 GHz line, which have the same quantum numbers, are in the frequency coverage of ALMA Band 5 (Immer et al. 2016; Humphreys et al. 2017), and the para-$H_2{}^{16}O$ 325 GHz line and the para-$H_2{}^{18}O$ 322 GHz line, which have the same transition levels, are in ALMA Band 7. The candidate ortho-$H_2{}^{16}O$ 321 GHz line (see Paper II) is also in ALMA Band 7. Since their line fluxes are larger than those of other water lines at similar wavelengths and the atmospheric conditions of ALMA Bands 5 and 7 are usually better than those at shorter wavelengths, they are suitable for tracing the hot water gas inside the H_2O snowline. Because of the small values of E_{up}, the para-$H_2{}^{16}O$ lines at 183 and 325 GHz are strongly affected by atmospheric absorption. By contrast, the effects of atmospheric absorption are less in the cases of $H_2{}^{18}O$ lines, and $H_2{}^{16}O$ lines with larger values of E_{up} ($\sim$1000–2000 K).

Other submillimeter ortho- and para-H_2O lines that trace the H_2O snowline exist in ALMA Bands 8, 9, and 10 ($\sim$275–950 GHz, see also Figures 7 and 8, Tables 3 and 4). The number of candidate water lines is largest in ALMA Band 8, which has three ortho-$H_2{}^{16}O$ lines, four para-$H_2{}^{16}O$ lines, and one ortho-$H_2{}^{18}O$ line. The values of A_{ul} are around (1–7) $\times$ 10^{-5} s^{-1}, and the values of E_{up} range from 300 K to 1600 K. The ortho-$H_2{}^{16}O$ 621 GHz and the ortho-$H_2{}^{18}O$ 692 GHz lines are transitions from the same energy levels and both fall in Band 9. Two candidate para-$H_2{}^{16}O$ lines and one para-$H_2{}^{18}O$ line fall in ALMA Band 10. Here we note that the $H_2{}^{16}O$ lines with small values of E_{up} ($<$1000 K) are strongly affected by atmospheric absorption.

There are no candidate $H_2{}^{16}O$ and $H_2{}^{18}O$ lines within the frequency coverage of ALMA Bands 3 and 4. The ortho-$H_2{}^{18}O$ 254 GHz line is in Band 6 and it has the same transition energy level of ortho-$H_2{}^{16}O$ 321 GHz line (see Paper II), although it has a relatively larger value of E_{up} ($=$1853.5 K) and its fluxes are relatively smaller than those of Band 5 and 7 lines.

Although we predict that the fluxes of the submillimeter candidate lines are too small in T Tauri disks ($\sim 10^{-23}$–10^{-22} W m^{-2}) to detect with a reasonable integration time with current ALMA sensitivity ($\sim 10^{-21}$–10^{-20} W m^{-2}; 5σ, 1 hr), the

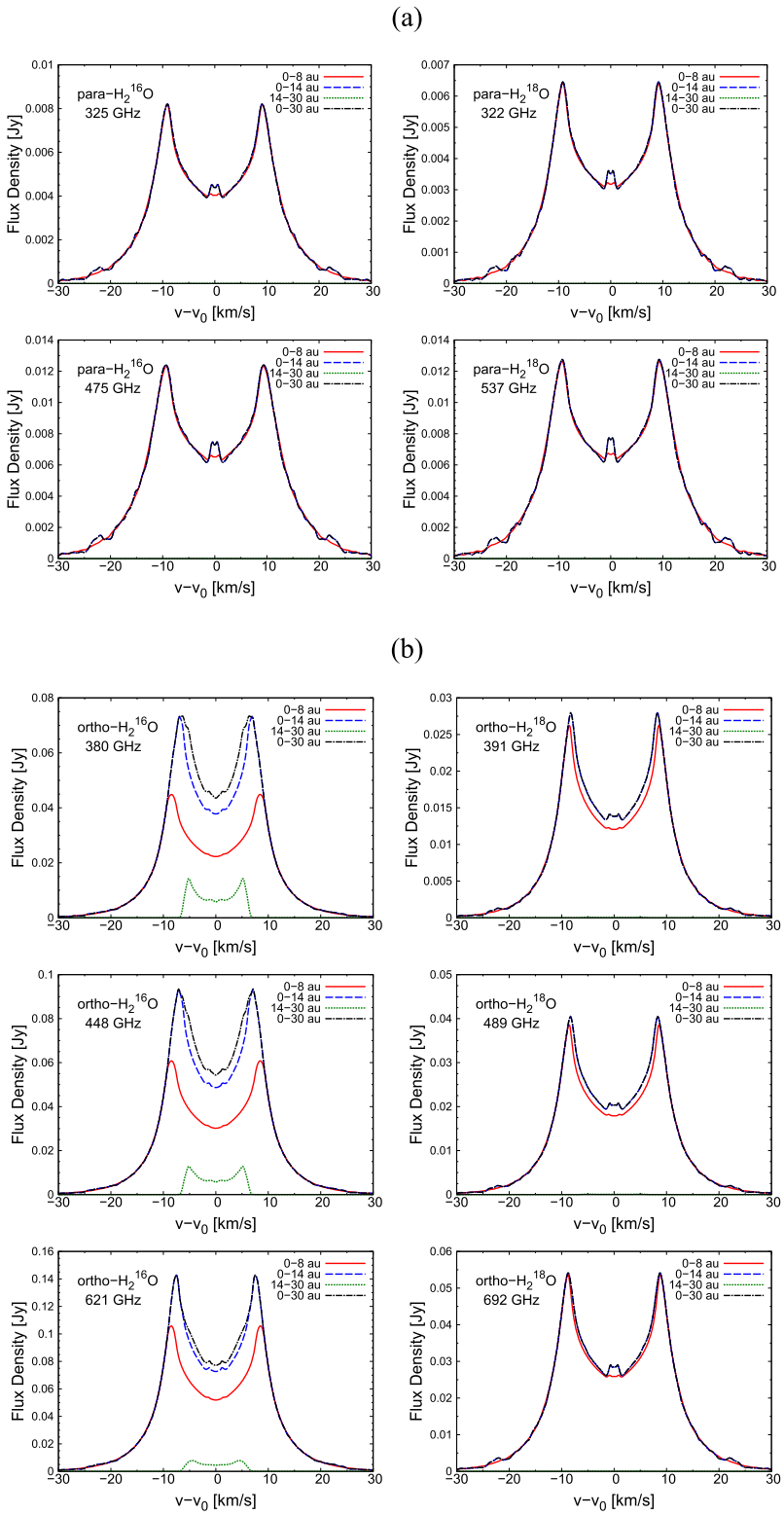

Figure 8. (a) The profiles of para-$H_2{}^{16}O$ lines at 325 GHz (top left) and 475 GHz (bottom left), and para-$H_2{}^{18}O$ lines at 322 GHz (top right), and 537 GHz (bottom right) from the Herbig Ae disk. The parameters and total fluxes of these H_2O lines are listed in Tables 3 and 4. In these profiles, we do not include dust emission. The line profiles from within 8 au, the inner high-temperature region, are displayed with red solid lines, those from within the H_2O snowline, 14 au, with blue dashed lines, those from 14 to 30 au, outside the H_2O snowline, with green dotted lines, and those from the total area inside 30 au, with black dashed dotted lines. In the panels of para-$H_2{}^{16}O$ and para-$H_2{}^{18}O$ line profiles, the flux densities outside the H_2O snowline (green dotted lines, $<10^{-4}$ Jy) are much smaller than those inside 8 au (red solid lines). Therefore, the red solid lines, blue dashed lines, and black dashed dotted lines are almost completely overlapped (see also Figure 1). (b) The profiles of ortho-$H_2{}^{16}O$ lines at 380 GHz (top left), 448 GHz (middle left), and 621 GHz (bottom left), ortho-$H_2{}^{18}O$ lines at 391 GHz (top right), 489 GHz (middle right), and 692 GHz (bottom right) from the Herbig Ae disk. The parameters and total fluxes of these H_2O lines are listed in Tables 3 and 4. In the panels of ortho-$H_2{}^{18}O$ line profiles, the flux densities outside the H_2O snowline (green dotted lines, $<10^{-3}$ Jy) are much smaller than those inside 8 au (red solid lines). Therefore, the red solid lines, blue dashed lines, and black dashed dotted lines are almost completely overlapped (see also Figure 1).

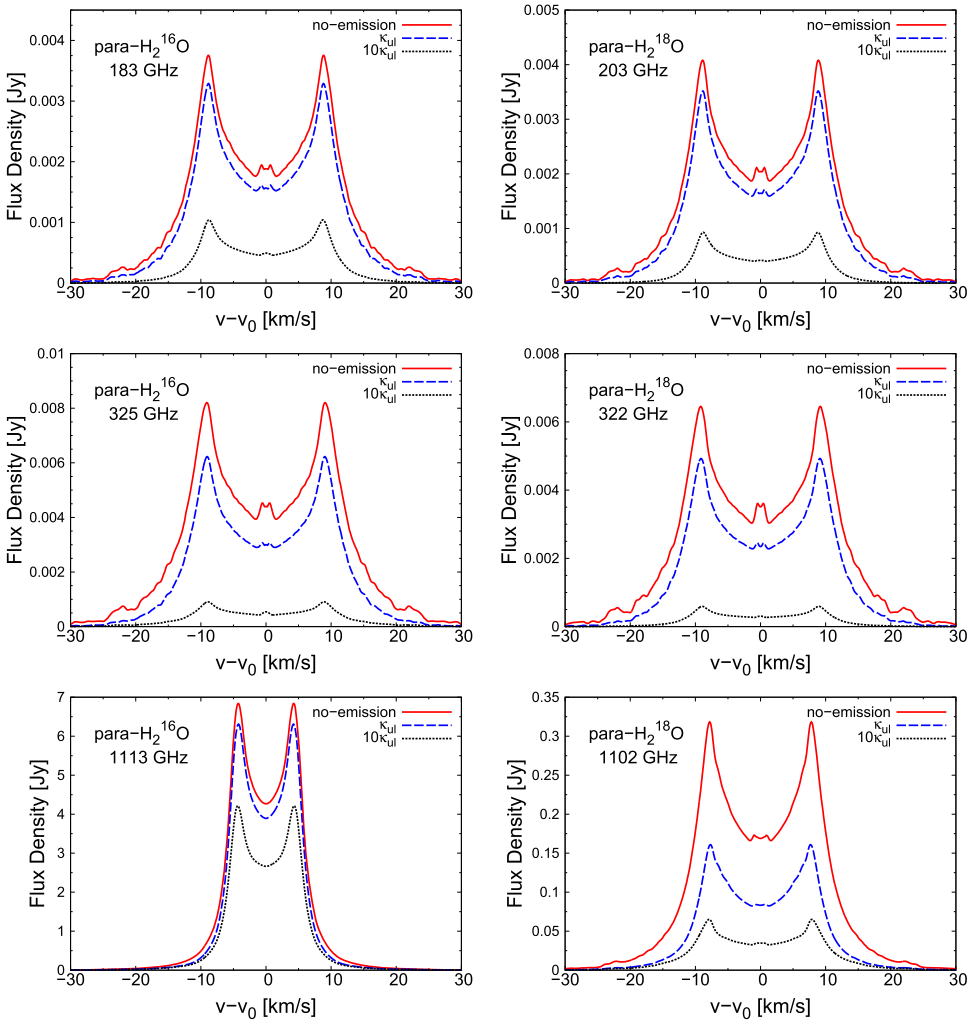

Figure 9. Profiles of para-$H_2{}^{16}O$ lines at 183 GHz (top left), 325 GHz (middle left), and 1113 GHz (bottom left), and para-$H_2{}^{18}O$ lines at 203 GHz (top right), 322 GHz (middle right), and 1102 GHz (bottom right) from a Herbig Ae disk inside 30 au. In the line profiles with red solid lines, we do not include dust emission components (see also Figures 1 and 8). In the line profiles with blue dashed lines and black dotted lines, we include both dust and gas emission components, and we subtract dust emission components (the values of fluxes at $v - v_0 = \pm\infty$) after the calculation to show the line emission component more clearly. In the line profiles with black dotted lines, we set the values of dust opacity $\kappa_{\rm ul}$ 10 times larger in order to investigate the influence of dust opacity on line properties.

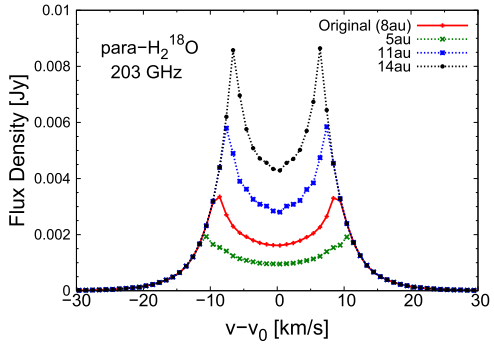

Figure 10. Profiles of the para-$H_2{}^{18}O$ line at 203 GHz from a Herbig Ae disk inside 30 au with a reduced velocity resolution ($\Delta v = 1.0$ km s^{-1}). When we calculate these line profiles, we include both dust and gas emission components, and we subtract dust emission components (the values of fluxes at $v - v_0 = \pm\infty$) after calculations to show the line emission component more clearly. The red solid line with cross symbols is the line profile of our original Herbig Ae disk model (see also Figure 9). In other plots, we artificially change the outer edge of the region with a high H_2O water gas abundance ($\sim 10^{-5}$–10^{-4}) region to 5 au (the green dotted line with cross symbols), 11 au (the blue dotted line with square symbols), and 14 au (the black dotted line with circle symbols).

fluxes are relatively strong and a greater possibility of successful detections are expected in Herbig Ae disks, in T Tauri disks with younger ages (e.g., HL Tau, ALMA Partnership et al. 2015; Banzatti et al. 2015; Harsono et al. 2015; Zhang et al. 2015; Okuzumi et al. 2016), and in disks around FU Orionis–type stars (e.g., V883 Ori, Cieza et al. 2016; Schoonenberg et al. 2017). The predicted fluxes of the para-$H_2{}^{16}O$ 183 GHz (Band 5), para-$H_2{}^{18}O$ 203 GHz (Band 7), para-$H_2{}^{16}O$ 325 GHz (Band 7), and para-$H_2{}^{18}O$ 322 GHz (Band 7) lines are around 4×10^{-22}–10^{-21} W m^{-2} (see Tables 3 and 4). In addition, the fluxes of some water lines in Bands 8–9 are also estimated to be around 10^{-21}–10^{-20} W m^{-2} for a Herbig Ae disk (see also Tables 3 and 4).

Here we mention that the ortho-$H_2{}^{16}O$ 321 GHz line has been detected in the disk and outflow around the massive protostar candidate, Source I in Orion KL (Hirota et al. 2014), using ALMA, and around the embedded low-mass Class I protostar, HL Tau, using SMA (Kristensen et al. 2016). The interstellar para-$H_2{}^{16}O$ 183 GHz and the para-$H_2{}^{18}O$ 203 GHz lines were detected for the first time in the Orion and DR21 (OH) molecular clouds (e.g., Phillips et al. 1978). Some

previous observations reported the detections of the thermal para-$H_2{}^{18}O$ 203 GHz line toward hot molecular cloud cores and high-mass protostars (Jacq et al. 1988; van der Tak et al. 2006). Resolved detections of the thermal para-$H_2{}^{18}O$ 203 GHz line were reported toward the deeply embedded low-mass Class 0 protostars NGC 1333-IRAS4B (Jørgensen & van Dishoeck 2010), NGC 1333-IRAS2A, and NGC 1333-IRAS4A (Persson et al. 2012), using the IRAM Plateau de Bure Interferometer. They suggested that the water emission comes from the inner disk.

5. Conclusions

In this paper, we extended our previous work (Papers I and II, Notsu et al. 2016, 2017) on using the profiles of ortho-$H_2{}^{16}O$ lines for tracing the location of the H_2O snowline in a Herbig Ae disk and a T Tauri disk, to include submillimeter para-$H_2{}^{16}O$ and ortho- and para-$H_2{}^{18}O$ lines.

The number densities of the para-$H_2{}^{16}O$ molecules are around one-third smaller than that of ortho-$H_2{}^{16}O$, thus the para-$H_2{}^{16}O$ line can trace deeper into the disk than the ortho-$H_2{}^{16}O$ lines. Since the number densities of $H_2{}^{18}O$ molecules are around 560 times smaller than those of $H_2{}^{16}O$, they can probe deeper into the disk than the $H_2{}^{16}O$ lines (down to $z = 0$) and thus they are better candidates for detecting water emission within the H_2O snowline at the disk midplane. If the dust opacity of the disk is much larger than that adopted in our disk model, the $H_2{}^{16}O$ lines and lines with longer wavelengths are better candidates for submillimeter detection of the inner water reservoir. This is because the dust opacity becomes larger as the line frequency increases. In addition, the temperature is higher as the disk height is higher and thus the temperature around $\tau_{\rm ul} \sim 1$ of $H_2{}^{16}O$ lines is higher than those of $H_2{}^{18}O$ lines. Therefore, the line intensities are larger in the case of $H_2{}^{16}O$ lines, compared with the case of $H_2{}^{18}O$ lines. The values of the Einstein A coefficients of submillimeter candidate water lines tend to be smaller (typically $<10^{-4}\,{\rm s}^{-1}$) than infrared candidate water lines (see Paper II). Thus, in the case of submillimeter candidate water lines, the local intensity from the outer optically thin region in the disk is around 10^4 times smaller than that in infrared candidate water line cases (see Paper II). Therefore, in the case of submillimeter lines, especially for $H_2{}^{18}O$ and para-$H_2{}^{16}O$, lines with relatively smaller upper state energies (∼a few 100 K) can also be used to trace the location of the water snowline. The values of candidate water line fluxes of the T Tauri disk are around $(1–5) \times 10^2$ smaller than those of the Herbig Ae disk, because the location of the H_2O snowline in the T Tauri disk exists at a smaller radius from the star than that in the Herbig Ae disk.

There are several candidate water lines that trace the hot water gas inside the H_2O snowline in ALMA Bands 5–10. The successful detection of candidate water lines in Herbig Ae disks and younger T Tauri disks could be achieved with current ALMA capabilities.

We are grateful to Professor Hiroshi Shibai and Professor Inga Kamp for their useful comments. We thank the referee for many important suggestions and comments. Our numerical studies were carried out on SR16000 at Yukawa Institute for Theoretical Physics (YITP) and computer systems at Kwasan and Hida Observatory (KIPS) in Kyoto University, and PC cluster at Center for Computational Astrophysics, National Astronomical Observatory of Japan. This work is supported by JSPS (Japan Society for the Promotion of Science) Grants-in-Aid for Scientific Research (Grant Number; 25108004, 25108005, 25400229, 15H03646, 15K17750), by Grants-in-Aid for JSPS fellows (Grant Number; 16J06887), and by the Astrobiology Center Program of National Institutes of Natural Sciences (NINS; Grant Number AB281013). S.N. is grateful for the support from the educational program organized by Unit of Synergetic Studies for Space, Kyoto University. C.W. acknowledges support from the Netherlands Organization for Scientific Research (NWO, program number 639.041.335) and start-up funds from the University of Leeds. Astrophysics at Queen's University Belfast is supported by a grant from the STFC (ST/P000312/1).

Software: RATRAN (Hogerheijde & van der Tak 2000).

ORCID iDs

Shota Notsu https://orcid.org/0000-0003-2493-912X
Hideko Nomura https://orcid.org/0000-0002-7058-7682
Catherine Walsh https://orcid.org/0000-0001-6078-786X
Mitsuhiko Honda https://orcid.org/0000-0002-6172-9124
Tomoya Hirota https://orcid.org/0000-0003-1659-095X
Eiji Akiyama https://orcid.org/0000-0002-5082-8880
T. J. Millar https://orcid.org/0000-0001-5178-3656

References

Aikawa, Y., & Nomura, H. 2006, ApJ, 642, 1152
ALMA Partnership, Brogan, C. L., Pérez, L. M., et al. 2015, ApJL, 808, L3
Antonellini, S., Bremer, J., Kamp, I., et al. 2017, A&A, 597, A72
Antonellini, S., Kamp, I., Lahuis, F., et al. 2016, A&A, 585, A61
Antonellini, S., Kamp, I., Riviere-Marichalar, P., et al. 2015, A&A, 582, A105
Banzatti, A., Meyer, M. R., Bruderer, S., et al. 2012, ApJ, 745, 90
Banzatti, A., Pinilla, P., Ricci, L., et al. 2015, ApJL, 815, L15
Banzatti, A., Pontoppidan, K. M., Salyk, C., et al. 2017, ApJ, 834, 152
Blevins, S. M., Pontoppidan, K. M., Banzatti, A., et al. 2016, ApJ, 818, 22
Carr, J. S., & Najita, J. R. 2008, Sci, 319, 1504
Carr, J. S., & Najita, J. R. 2011, ApJ, 733, 102
Cieza, L. A., Casassus, S., Tobin, J., et al. 2016, Natur, 535, 258
Draine, B. T. 2006, ApJ, 636, 1114
Du, F., Bergin, E. A., Hogerheijde, M., et al. 2017, ApJ, 842, 98
Eistrup, C., Walsh, C., & van Dishoeck, E. F. 2016, A&A, 595, A83
Faure, A., & Josselin, E. 2008, A&A, 492, 257
Fedele, D., Bruderer, S., van Dishoeck, E. F., et al. 2012, A&A, 544, LL9
Fedele, D., Bruderer, S., van Dishoeck, E. F., et al. 2013, A&A, 559, AA77
Fedele, D., Pascucci, I., Brittain, S., et al. 2011, ApJ, 732, 106
Furuya, K., Aikawa, Y., Nomura, H., Hersant, F., & Wakelam, V. 2013, ApJ, 779, 11
Graedel, T. E., Langer, W. D., & Frerking, M. A. 1982, ApJS, 48, 321
Hama, T., Kouchi, A., & Watanabe, N. 2016, Sci, 351, 65
Hama, T., & Watanabe, N. 2013, ChRv, 113, 8783
Harsono, D., Bruderer, S., & van Dishoeck, E. F. 2015, A&A, 582, A41
Hayashi, C. 1981, PThPS, 70, 35
Hayashi, C., Nakazawa, K., & Nakagawa, Y. 1985, in Protostars and Planets II, ed. D. C. Black & M. S. Matthews (Tucson, AZ: Univ. Arizona Press), 1100
Heinzeller, D., Nomura, H., Walsh, C., & Millar, T. J. 2011, ApJ, 731, 115
Hirota, T., Kim, M. K., Kurono, Y., & Honma, M. 2014, ApJL, 782, L28
Hogerheijde, M. R., Bergin, E. A., Brinch, C., et al. 2011, Sci, 334, 338
Hogerheijde, M. R., & van der Tak, F. F. S. 2000, A&A, 362, 697
Honda, M., Inoue, A. K., Fukagawa, M., et al. 2009, ApJL, 690, L110
Honda, M., Kudo, T., Takatsuki, S., et al. 2016, ApJ, 821, 2
Honda, M., Maaskant, K., Okamoto, Y. K., et al. 2015, ApJ, 804, 143
Humphreys, E., Biggs, A., Immer, K., et al. 2017, Msngr, 167, 7
Ida, S., & Guillot, T. 2016, A&A, 596, L3
Immer, K., Belitsky, V., Olberg, M., et al. 2016, Msngr, 165, 13
Inoue, A. K., Honda, M., Nakamoto, T., & Oka, A. 2008, PASJ, 60, 557
Jacq, T., Henkel, C., Walmsley, C. M., Jewell, P. R., & Baudry, A. 1988, A&A, 199, L5
Jørgensen, J. K., & van Dishoeck, E. F. 2010, ApJL, 710, L72
Kamp, I., Thi, W.-F., Meeus, G., et al. 2013, A&A, 559, A24
Krijt, S., Ciesla, F. J., & Bergin, E. A. 2016, ApJ, 833, 285

Kristensen, L. E., Brown, J. M., Wilner, D., & Salyk, C. 2016, ApJL, 822, L20
Mandell, A. M., Bast, J., van Dishoeck, E. F., et al. 2012, ApJ, 747, 92
Mathis, J. S., Rumpl, W., & Nordsieck, K. H. 1977, ApJ, 217, 425
Meeus, G., Montesinos, B., Mendigutía, I., et al. 2012, A&A, 544, AA78
Meijerink, R., Poelman, D. R., Spaans, M., Tielens, A. G. G. M., & Glassgold, A. E. 2008, ApJL, 689, L57
Meijerink, R., Pontoppidan, K. M., Blake, G. A., Poelman, D. R., & Dullemond, C. P. 2009, ApJ, 704, 1471
Miyake, K., & Nakagawa, Y. 1993, Icar, 106, 20
Morbidelli, A., Bitsch, B., Crida, A., et al. 2016, Icar, 267, 368
Morbidelli, A., Chambers, J., Lunine, J. I., et al. 2000, M&PS, 35, 1309
Morbidelli, A., Lunine, J. I., O'Brien, D. P., Raymond, S. N., & Walsh, K. J. 2012, AREPS, 40, 251
Mumma, M. J., Weaver, H. A., & Larson, H. P. 1987, A&A, 187, 419
Najita, J. R., Carr, J. S., Pontoppidan, K. M., et al. 2013, ApJ, 766, 134
Nomura, H., Aikawa, Y., Tsujimoto, M., Nakagawa, Y., & Millar, T. J. 2007, ApJ, 661, 334
Nomura, H., & Millar, T. J. 2005, A&A, 438, 923
Notsu, S., Nomura, H., Ishimoto, D., et al. 2015, in ASP Conf. Ser. 499, Revolution in Astronomy with ALMA: The Third Year, ed. D. Iono et al. (Francisco, CA: ASP), 289
Notsu, S., Nomura, H., Ishimoto, D., et al. 2016, ApJ, 827, 113 (Paper I)
Notsu, S., Nomura, H., Ishimoto, D., et al. 2017, ApJ, 836, 118 (Paper II)
Öberg, K. I., Murray-Clay, R., & Bergin, E. A. 2011, ApJL, 743, L16
Oka, A., Nakamoto, T., & Ida, S. 2011, ApJ, 738, 141
Okuzumi, S., Momose, M., Sirono, S.-i., Kobayashi, H., & Tanaka, H. 2016, ApJ, 821, 82
Okuzumi, S., Tanaka, H., Kobayashi, H., & Wada, K. 2012, ApJ, 752, 106
Persson, M. V., Jørgensen, J. K., & van Dishoeck, E. F. 2012, A&A, 541, A39
Phillips, T. G., Scoville, N. Z., Kwan, J., Huggins, P. J., & Wannier, P. G. 1978, ApJL, 222, L59
Pinilla, P., Pohl, A., Stammler, S. M., & Birnstiel, T. 2017, ApJ, 845, 68
Piso, A.-M. A., Öberg, K. I., Birnstiel, T., & Murray-Clay, R. A. 2015, ApJ, 815, 109
Piso, A.-M. A., Pegues, J., & Öberg, K. I. 2016, ApJ, 833, 203
Podio, L., Kamp, I., Codella, C., et al. 2013, ApJL, 766, L5
Pontoppidan, K. M., Salyk, C., Blake, G. A., et al. 2010a, ApJ, 720, 887
Pontoppidan, K. M., Salyk, C., Blake, G. A., & K&aumlufl, H. U. 2010b, ApJL, 722, L173
Raymond, S. N., & Izidoro, A. 2017, Icar, 297, 134
Riviere-Marichalar, P., Ménard, F., Thi, W. F., et al. 2012, A&A, 538, L3
Ros, K., & Johansen, A. 2013, A&A, 552, A137
Rothman, L. S., Gordon, I. E., Babikov, Y., et al. 2013, JQSRT, 130, 4
Rybicki, G. B., & Lightman, A. P. 1986, in Radiative Processes in Astrophysics, ed. G. B. Rybicki & A. P. Lightman (New York: Wiley-VCH), 400
Salinas, V. N., Hogerheijde, M. R., Bergin, E. A., et al. 2016, A&A, 591, A122
Salyk, C., Pontoppidan, K. M., Blake, G. A., et al. 2008, ApJL, 676, L49
Salyk, C., Pontoppidan, K. M., Blake, G. A., Najita, J. R., & Carr, J. S. 2011, ApJ, 731, 130
Sato, T., Okuzumi, S., & Ida, S. 2016, A&A, 589, A15
Schöier, F. L., van der Tak, F. F. S., van Dishoeck, E. F., & Black, J. H. 2005, A&A, 432, 369
Schoonenberg, D., Okuzumi, S., & Ormel, C. W. 2017, A&A, 605, L2
van der Tak, F. F. S., Walmsley, C. M., Herpin, F., & Ceccarelli, C. 2006, A&A, 447, 1011
van Dishoeck, E. F., Bergin, E. A., Lis, D. C., & Lunine, J. I. 2014, in Protostars and Planets VI, ed. H. Beuther et al. (Tucson, AZ: Univ. Arizona Press), 835
van Kempen, T. A., Doty, S. D., van Dishoeck, E. F., Hogerheijde, M. R., & Jørgensen, J. K. 2008, A&A, 487, 975
Walsh, C., Millar, T. J., & Nomura, H. 2010, ApJ, 722, 1607
Walsh, C., Millar, T. J., Nomura, H., et al. 2014, A&A, 563, AA33
Walsh, C., Nomura, H., Millar, T. J., & Aikawa, Y. 2012, ApJ, 747, 114
Walsh, C., Nomura, H., & van Dishoeck, E. 2015, A&A, 582, A88
Walsh, K. J., Morbidelli, A., Raymond, S. N., O'Brien, D. P., & Mandell, A. M. 2011, Natur, 475, 206
Weingartner, J. C., & Draine, B. T. 2001, ApJ, 548, 296
Wilson, T. L., & Rood, R. 1994, ARA&A, 32, 191
Woitke, P., Thi, W.-F., Kamp, I., & Hogerheijde, M. R. 2009b, A&A, 501, L5
Woodall, J., Agúndez, M., Markwick-Kemper, A. J., & Millar, T. J. 2007, A&A, 466, 1197
Zhang, K., Blake, G. A., & Bergin, E. A. 2015, ApJL, 806, L7
Zhang, K., Pontoppidan, K. M., Salyk, C., & Blake, G. A. 2013, ApJ, 766, 82